EIF6 conditions drug-tolerant persister-like transdifferentiation in small cell lung carcinoma

Shensi Shen

shensi.sean@gmail.com

West China hospital, Sichuan University https://orcid.org/0000-0002-5087-8220

Haoning Peng

West China Hospital, Sichuan University https://orcid.org/0000-0003-1388-3255

Zhile Wang

Sichuan University https://orcid.org/0000-0001-6820-8383

Mengyao Wang

West China hospital, Sichuan University

Xinpu Tang

West China hospital, Sichuan University

Kaixiu Li

West China hospital, Sichuan University

Xuejiao Yu

West China hospital, Sichuan University

Siyang Song

West China hospital, Sichuan University

Yuqing Wang

West China hospital, Sichuan University

Tianjian Lu

West China hospital, Sichuan University

Bo Dong

West China hospital, Sichuan University

Youyu Wang

Sichuan University

Minqi Chen

Sichuan University

Dongjian Ceng

West China hospital,Sichuan University

Yulan Deng

West China hospital,Sichuan University

Liang Xia

West China hospital,Sichuan University

Chenglin Guo

West China hospital,Sichuan University

Qiang Pu

West China Medical Center

Lu Li

Lung Cancer Center, West china Hospital, Sichuan University

Michael Cerezo

INSERM, U1065, Equipe 12, Centre Méditerranéen de Médecine Moléculaire https://orcid.org/0000-0002-3687-2009

Weiya Wang

West China hospital, Sichuan University

Lunxu Liu

West China hospital, Sichuan University

Biological Sciences - Article

Keywords:

Posted Date: May 30th, 2024

DOI: https://doi.org/10.21203/rs.3.rs-4232167/v1

Additional Declarations: Yes there is potential Competing Interest. M.C. is a CSO for BiPer Therapeutics (Strasbourg, France). S.S. reports personal fees from Agence nationale de la recherche (France), Krebsliga Schweiz (Switzerland), KWF Kankerbestrijding (Netherlands) and Shenzhen Medical Academy of Research and Translation (China).

Abstract

Drug-tolerant persister cells withstand treatments by adapting their identity through lineage-dependent plasticity during systemic anti-cancer therapies. This phenomenon is evident in small-cell lung carcinoma (SCLC), a lethal neuroendocrine cancer initially responsive (60-80%) to platinum-based chemotherapy but succumbing to resistance within 6 months in advanced stages. This resistance associates with the transdifferentiation of residual tumour cells into a non-neuroendocrine state, a process intricately tied to SCLC's chemotolerance, yet molecular mechanisms governing this lineage conversion remain completed understood. Here we report that first-line chemotherapy induces translation initiation factor eIF6 in drug-tolerant persister-like cells in SCLC, associating with the non-neuroendocrine state in both SCLC genetically engineered mouse model and patient samples. Intervening eIF6 inhibits non-neuroendocrine transdifferentiation, thus enhancing SCLC responsiveness to chemotherapy. Mechanistically, therapy-induced eIF6 dissociates from ribosomes whereas interacts with the extracellular matrix complex CD104/FAK, leading to the activation of MAPK pathway and a global translational remodelling in SCLC drug-tolerant persister-like cells. This prompts us to develop an eIF6-CD104/FAK proximity ligation assay applicable to clinical samples, showing its prognostic value for SCLC clinical outcomes. This study of eIF6's moonlight function sheds light on its potential therapeutic interventions to mitigate treatment resistance in SCLC.

Introduction

Drug-tolerant persister (DTP) cells survive in cancers initially responsive to anti-cancer treatment, contributing significantly to treatment failure[1]. Owing to their considerable plasticity[5,6], DTP cells can alter their identity in a lineage-dependent manner to shield themselves from therapeutic targeting[7]. SCLC, a high-grade neuroendocrine (NE) cancer, displays notable cellular plasticity and heterogeneity[8]. Transdifferentiation of neuroendocrine SCLC into a non-NE state increases its intra-tumoral diversity, fostering resistance to initial chemotherapy[9]. Approximately 20% of SCLC cases exhibit a loss of the NE phenotype[10]. Various mechanisms, including YAP1[11] or MYC[12] transcriptional regulation, KDM6A epigenetic regulation[13], or Notch pathway upregulation[14], contribute to this transdifferentiation, representing a continuum through which residual SCLC cells can evolve and evade therapy. Nevertheless, additional mechanisms governing this lineage conversion remain elusive. We previously demonstrated that melanoma DTP cells undergo significant translational remodelling to promote treatment tolerance[15,16]. Here we report that first-line chemotherapy triggers a non-classical role of translation initiation factor eIF6, conditioning SCLC DTP-like transdifferentiation to endorse chemotolerance.

Translational remodelling in chemotolerant SCLC

The extensive-stage SCLC has a median overall survival of 8 to 12 months, with a 5-year survival rate less than 2%[17]. Despite the swift and remarkable responses to initial therapy, relapse is common, posing a significant challenge in managing this persistent cancer[3]. Studies on human samples have been

unable to detect significant mutational differences between treatment-naïve and relapsed SCLC[14,18–20], emphasizing the role of non-genetic plasticity in drug tolerance. To further investigate the chemotolerance of SCLC cells, we conducted a comparative analysis of gene expression profiles between relapsed SCLC patient samples post-chemotherapy (n = 18)[14] and treatment-naïve SCLC samples (n = 81)[21] using single-sample gene set enrichment analysis (ssGSEA)[22] (Fig. 1a). Enrichment of pathways related to eukaryotic translation and 60S ribosome regulation was observed in relapsed samples (Fig. 1b), hinting at translation regulation in SCLC's chemotherapy tolerance. Similar enrichment occurred in *ASCL1*^{low}/*NEUROD1*^{low} non-NE SCLC cells[23] refractory to chemotherapy and anti-PDL1 immunotherapy in IMPower 133 trial[24] (**Extended data** Fig. 1a, b). Indeed, chemosensitive SCLC cell line H69 treated with carboplatin and etoposide for three days showed a subset with a DTP-like feature surviving treatment with a known variant non-NE phenotype where cells transitioned from suspension culture to attached growth. These DTP-like SCLC cells displayed increased tolerance to the same chemotherapy compared to their parental counterparts (**Extended data** Fig. 1c, d). Similarly, the resistant SCLC cell line H196, characterized by a non-NE attached growth phenotype, also demonstrated slightly increased drug tolerance in residual cells compared to the parental cells (**Extended data** Fig. 1d). In accordance, post-treatment H69 and H196 cells exhibited increased expression of mesenchymal markers such as vimentin and YAP1, while NE-associated proteins like N-myc and ASCL1were downregulated compared to three other ASCL1^{+} or NEUROD1^{+} SCLC cell lines (**Extended data** Fig. 1e). This chemotherapy tolerance was also confirmed in an induced non-NE model, where H69 cells underwent transdifferentiation into a non-NE phenotype (H69M) following the treatment with Hepatocyte growth factor (HGF)[25,26] (**Extended data** Fig. 1f-h).

In line with our transcriptomic analysis, the chemotolerant non-NE cells exhibited a significant alteration in translation activity compared to their NE counterparts, as revealed by polysome profiling[15]. Ultracentrifugation of H69M cell lysates on a sucrose gradient indicated a reduced content of polysome-bound mRNAs compared to H69 cells (Fig. 1c). Additionally, ribosomal proteins from both large and small subunit ribosomes extracted from each fraction displayed a shift toward monosomes (Fig. 1d). Similar trends were observed in H196 chemotolerant non-NE cells (**Extended data** Fig. 2a). Concurrent with these polysome profile changes, we noted an increase in the phosphorylation of RPS6 (p-RPS6) in non-NE SCLC cells compared to NE cells (**Extended data** Fig. 2b). This elevated p-RPS6 consistently associated with poly-ribosomes in non-NE cell lysates (**Extended data** Fig. 2c, d), whose dephosphorylation is recognized as necessary for actively translating ribosomes[27]. Transcriptomic pathway analysis also confirmed the transdifferentiated non-NE state (**Extended data** Fig. 2e **and Supplementary Table 3**). Collectively, translation remodelling in chemotolerant cells may be linked to the non-NE lineage conversion in SCLC, a connection that remains unexplored.

Translation landscape in NE versus non-NE SCLC

To elucidate the translational landscape of SCLC during DTP-like transdifferentiation, we conducted genome-wide polysome profiling analyses to identify mRNAs under translational regulation (Fig. 1e).

Through polysome-associated RNA sequencing in H69M and H69 cells, we categorized mRNAs in three groups: group 1 exhibited at least a twofold change in cytoplasmic mRNA levels but less than a twofold change in polysomal mRNA levels (Fig. 1f, blue points); group 2 showed at least a twofold change in polysomal mRNA levels but less than a twofold change in cytoplasmic mRNA levels (Fig. 1f, orange points); group 3 displayed at least a twofold change, either an increase or decrease, in both cytoplasmic and polysomal mRNA levels (Fig. 1f, green points). This paired transcription-translation analysis unveiled significant alterations in translational regulation along the spectrum of SCLC transdifferentiation. Similar findings were replicated in H196 cells when compared to H69 cells (**Extended data** Fig. 3a **and Supplementary Table 1**). Notably, differentially expressed (ΔmRNA, FDR < 1% and $\log_2|FC| > 1$) or differentially translated (Δtranslation efficiency [ΔTE], FDR < 10%) events occur largely independent of each other, demonstrating minimal overlaps between changes in translation and transcription resulting from the non-NE cell state compared to the NE cell state (Fig. 1g and **Extended data** Fig. 3b). Specifically, transcripts associated with neuroendocrine transdifferentiation were revealed to be regulated at translational level; for instance, transcripts related to NE cell state were downregulated (*CHGB, TFF3, INSM1, ASCL1, MYCN* etc), while transcripts related to non-NE cell state were upregulated (*CAV1, NOTCH3, VIM, YAP1* etc) (Fig. 1h and **Extended data** Fig. 3c).

The observed global downregulation of translation in non-NE cell state may be linked to alterations in ribosome scanning or its composition triggered by cellular stress response[28,29]. We firstly measured ribosome transit rate through a harringtonine run-off assay (**Extended data** Fig. 3d)[30]. Treatment of harringtonine to both NE and non-NE cells led to a decrease in polysomes and an augmentation in 80S ribosomes (**Extended data** Fig. 3e), thus ruling out ribosome stalling as the underlying cause of the global translation remodelling. We subsequently employed quantitative high-coverage tandem-mass-tag (TMT) mass spectrometry in SCLC cells to assess the expression of all ribosome proteins (RPs) (**Extended data** Fig. 4a **and Supplementary Table 2**)[31]. Cells were fractioned using sucrose gradient sedimentation, and monosomes (M, a single ribosome), light polysomes (LP, 2–4 ribosomes), and heavy polysomes (HP, ≥ 5 ribosomes) were collected from both H69 and H69M cells (Fig. 1i). On average, we detected peptides predominantly in the range of 8–20 amino acids, with a high protein coverage (**Extended data** Fig. 4b-d). A diverse array of subcellular proteins potentially associated with polysomes was detected, with a substantial proportion belonging to nucleus proteins (37%) (**Extended data** Fig. 4e). Gene ontology analysis showed an enrichment of translation-related components in our mass spectrometry analysis (**Extended data** Fig. 4f). Consistent with our polysome RNAseq, differential expression analysis demonstrated distinct protein expression profiles associated with ribosomes in each sub-fraction (**Extended data** Fig. 4g). Moreover, principal component analysis highlighted a clear distinction between NE and non-NE cell states, emphasizing translation remodelling during SCLC transdifferentiation (Fig. 1j). Intriguingly, while a global downregulation of translation activity was observed in non-NE cell state compared to NE cell state, the average composition of RPs within monosomes, light polysomes, and heavy polysomes remained largely invariant (Fig. 1k). These results suggest that translation alterations associated with SCLC transdifferentiation may result from regulatory mechanisms other than the stalling or the formation of ribosomes with distinct protein compositions.

Chemotherapy-induced eIF6 expression anti-correlates with NE cell state in SCLC

In addition to the overarching reduction in polysome fractions, a discernible elevation in the abundance of 60S ribosomal subunit was noted in non-NE cell state relative to NE cell state (Fig. 1). The eIF6 interacts with nascent 60S subunits, aiding assembly with 40S subunits for active translation[32]. Elevated eIF6 in c-Kit + bone marrow cells reduces the 80S:60S ratio, deactivating translating 80S ribosomes[33]. This designates eIF6 as a rate-limiting enzyme in mouse and human tumorigenesis, evident in studies with *Eif6*$^{+/-}$ mouse embryonic fibroblasts showing reduced transformation activity[34]. Following exposure to carboplatin/etoposide, we consistently observed upregulation of eIF6 expression in human SCLC cell lines (Fig. 2a and **Extended data Fig. 5a**), as well as in mouse tumour cell line derived from *Rb1*$^{-/-}$*/Trp53*$^{-/-}$*/Myc*^{T58A} (RPM)[35] mouse SCLC model (**Extended data Fig. 5b**). Similarly, the expression of eIF6 protein exhibited an upregulation in chemotolerant non-NE cell state when compared to the sensitive NE cell state (Fig. 2b and **Extended data Fig. 5c**). To further explore whether eIF6 expression experiences an upregulation in residual disease settings, we subjected *Balb/cNj-Foxn1*^{nu}*/Gpt* mice subcutaneously transplanted with human H69 SCLC cells to carboplatin/etoposide treatment (Fig. 2c, top). A swift response was observed during the regression phase; however, tumours relapsed around ~ 60 days upon treatment, following a minimal residual phase (Fig. 2c, bottom). Tumour tissues were collected from four representative phases, including untreated samples, regression phase, minimal residual phase and regrowth phase. Intriguingly, eIF6 protein expression was exclusively upregulated during the minimal residual phase, mirroring our *in vitro* observations (Fig. 2d and **Extended data Fig. 5d**). In line with our *in vivo* findings, eIF6 expression demonstrated an anti-correlation with the expression NE cell state-related transcription factors, such as *ASCL1* and *NEUROD1*, in a patient cohort undergoing chemotherapy[14] (**Extended data Fig. 5e**).

Recent studies propose categorizing small-cell lung cancer (SCLC) into subtypes based on distinct transcription factor expressions: ASCL1 (SCLC-A), NEUROD1 (SCLC-N), POU2F3 (SCLC-P), and their inflammatory profiles (SCLC-I)[36]. The ASCL1-defined SCLC-A, comprising 40–50% of cases, is pathologically associated with the neuroendocrine (NE) cell state[37]. SCLC-N, initially defined as a separate subtype expressing NEUROD1, shares NE cell state association with SCLC-A but has lower overall NE marker expression[38]. SCLC-P tumours, with elevated POU2F3 and increased Myc expression, represent a distinct non-NE variant refractory to chemotherapy[39]. Given the chemotherapy-induced upregulation of eIF6 expression in non-NE SCLC cell lines, we performed an analysis of SCLC patient samples, categorizing them into four groups based on the expression of classical NE-associated TFs, namely ASCL1^{high}, NEUROD1^{high}, dual-positive (ASCL1^{high}NEUROD1^{high}) and dual-negative (ASCL1^{low}NEUROD1^{low}). Notably, the expression of eIF6 was significantly increased in the dual-negative samples, suggesting an anti-correlation between eIF6 expression and NE cell state in patient samples (Fig. 2e and **Extended data Fig. 5f**). Consistent with this, the expression of Myc, a known factor that promotes SCLC transdifferentiation[35], was also upregulated in non-NE tumour samples (**Extended data**

Fig. 5g-h). eIF6 release from the 60S ribosomal subunit requires SBDS, stimulating EFL1's GTPase activity and catalysing eIF6 removal from the cytoplasmic 60S subunit[40]. Despite observing an anti-correlation of eIF6 expression with NE cell state, the expression levels of SBDS or EFL1 did not exhibit significant changes (**Extended data Fig. 5i**).

To extend these findings, we conducted immunohistochemistry of Ascl1 and Eif6 in RPM mouse SCLC model, known for its NE-low histophathology[35]. Adenoviruses carrying *Cre*-driven by the neuroendocrine *calcitonin gene-related peptide* (*Cgrp*) promoter were nasally administered to mice (Fig. 2f). Micro-computed tomography revealed centrally located tumours with increased density at major bronchi between 5 and 7 weeks post-*Cgrp-Cre* infection (Fig. 2f). Eif6 staining intensified in the tumour bed, particularly in Ascl1-low regions, contrasting with lower Eif6 expression in Aslc1-high regions (Fig. 2f). Consistent with a study indicating reduced NE marker expression in invasive RPM tumours compared to $Rb1^{fl/fl}/Trp53^{fl/fl}/Rbl2^{fl/fl}$ (RPR2) mouse SCLC tumours[12], we observed heightened *Eif6* and *Myc* expression and relatively decreased *Ascl1* expression in RPM compared to RPR2 tumours (**Extended data Fig. 5j-k**). To investigate if comparable anti-correlation between eIF6 and NE cell state exists in patient samples, we collected a cohort of surgical specimens from limited stage SCLC patients (n = 38). We simultaneously detected ASCL1, NEUROD1 and eIF6 by utilizing multiplex immunofluorescence (mIF) on formalin-fixed, paraffin-embedded (FFPE) blocks (Fig. 2g), and developed a single-cell quantification of protein expression using QuPath software (Fig. 2g and **Extended data Fig. 6a**)[41]. Although there is a considerable intra-tumoural heterogeneity of the expression levels of ASCL1, NEUROD1 and eIF6, we found an anti-correlation between eIF6 and ASCL1 expression, consistent with our findings *in vitro* and in mice (Fig. 2h and **Extended data Fig. 6b**). Notably, even adjacent tumour cells exhibited varying expression levels of ASCL1 and eIF6, highlighting the dynamic regulation of eIF6 expression during transdifferentiation (**Extended data Fig. 6c**). This anti-correlation was further validated in the IMPower133 clinical trial RNA sequencing dataset (Fig. 2i), emphasizing the potential regulatory role of eIF6 in SCLC chemotolerant transdifferentiation.

Intervention of eIF6 sensitizes SCLC to chemotherapy

To assess the functional implications of chemotherapy-induced eIF6 upregulation in the evolution of drug response, we examined the impact of eIF6 knockdown in non-NE SCLC cells. RNA sequencing followed by gene set enrichment analysis (GSEA) revealed that eIF6 knockdown in H69M cells significantly downregulated epithelial-mesenchymal transition (EMT)-associated gene signatures (Fig. 3a and 3c), including NOTCH family proteins, integrin family proteins, and vimentin linked to EMT transdifferentiation in SCLC (Fig. 3c). Conversely, eIF6 knockdown markedly increased the neuroendocrine gene signature[42,43] (Fig. 3b **and Supplementary Table 3**), encompassing *HES6, TOP2A, DLL3, NEUROD1, ASCL1, INSM1* and *CHGA* (Fig. 3d **and Extended data 7a**). Despite no observable alterations in global translation activity upon eIF6 knockdown (**Extended data Fig. 7b**), a transdifferentiation assay[13] using RPM-derived mouse SCLC cell lines revealed distinct behaviours. Early-passage cell lines exhibited growth as neuroendocrine spheroid aggregates similar to human NE cells[35], while late-passage RPM mouse cell lines adopted an attached cell phenotype akin to a non-NE

variant (Fig. 3e). Remarkably, RPM mouse cell lines with eIF6 knockdown largely maintained a neuroendocrine spheroid aggregate configuration, suggesting a diminished capacity for transdifferentiation into a non-NE cell state (Fig. 3e). Extending on these findings, we replicated the assay in human H69 cell lines, known to transdifferentiate into a non-NE cell state upon HGF treatment[25]. As shown in **Extended data Fig. 7c**, H69 cells expressing non-targeted control shRNA (sh_NTC) exhibited increased attachment upon the treatment of HGF, evident in crystal violet staining. In contrast, eIF6 knockdown dramatically impeded this phenotypic change, maintaining cells as neuroendocrine spheroid aggregates in suspension, resulting in reduced percentage of crystal violet staining (**Extended data Fig. 7d**). This inhibitory effect of eIF6 knockdown was also evident in EZH2 inhibitor-mediated SCLC transdifferentiation[26] (**Extended data Fig. 7e**).

Given heightened sensitivity of neuroendocrine-state SCLC to platinum-based chemotherapy[44], we explored the potential of eIF6 knockdown in augmenting chemotherapy responsiveness across diverse models. First, human H69M cell line treatment with carboplatin/etoposide for 72 hours and subsequent flow cytometry analysis (**Extended data Fig. 7f-g**) revealed that eIF6 knockdown significantly reduced viable cell percentage compared to the non-targeted control upon chemotherapy (**Extended data Fig. 7h**). This effect was consistently observed in RPM-derived mouse SCLC cell line with Eif6 knockdown, leading to increased cell death during short-term chemotherapy treatment (**Extended data Fig. 7i**). Second, long-term treatment of carboplatin/etoposide, assessed by clonogenic assay[15], demonstrated that Eif6 knockdown in RPM-derived mouse SCLC cells not only reduced cell proliferation but also eliminated most residual persistent cells, as indicated by a significant reduction in remaining colonies (Fig. 3f). Notably, the enhanced responsiveness of SCLC to chemotherapy was further validated *in vivo*. Human H69 cell xenografts in *Balb/cNj-Foxn1^{nu}/Gpt* mice, following three cycles of carboplatin/etoposide treatment, exhibited disease progression in 76.9% of mice (PD, 10/13 mice) (Fig. 3g); In contrast, H69 cell xenografts with eIF6 knockdown displayed a disease response in 61.5% of mice, with 2 out of 13 mice showing a complete response (CR) and 6 out of 13 mice showing a partial response (PR) (Fig. 3g **and Extended data Fig. 7j**). Taken together, intervening eIF6 inhibits non-neuroendocrine transdifferentiation, thereby enhancing SCLC responsiveness to chemotherapy.

EIF6 moonlighting MAPK activation in non-NE chemotolerant SCLC

EIF6, a 245-amino acid conserved protein, shares 77% sequence identity between yeasts and humans[45]. At low concentrations, eIF6 mildly stimulates mRNA translation[46], whereas high concentrations inhibit translation[32]. *In vitro*, eIF6 presence increases 80S ribosome dissociation, preventing recycled ribosomal subunit re-association post-translation termination[47]. However, efficient recycling of free 60S ribosomal subunit requires eIF6 interaction, suggesting the need for tight regulation in eIF6's impact on mRNA translation[33]. To study the mechanisms underlying eIF6's role in SCLC persister-like transdifferentiation, we established an *in vitro* eIF6-ribosome binding assay using sucrose gradient ultracentrifugation[40]. Cell lysates underwent separation through sucrose gradient sedimentation, resulting in the pelleting of 60S

subunit-bound eIF6 (fraction F2) through a 30% sucrose cushion, while ribosome subunit-free eIF6 remained in fraction F1(Fig. 3g, top). Immunoblotting revealed a decreased abundance of eIF6 protein in the F2 fraction from non-NE cells (H69M) compared to their NE cell counterparts (H69) (Fig. 3g, bottom). Additionally, probing eIF6 distribution in the polysome profiles unveiled diminished levels of eIF6 protein in the 60S subunit-associated fractions (**Extended data Fig. 8a**). These findings indicate that chemotherapy-induced eIF6 in non-NE cell state undergoes dissociation from the ribosome pool.

We proceeded to analyse the eIF6 genome-wide interactome using BioGrid database[48], revealing its interaction with integrin β4 protein (ITGB4, also called CD104) (Fig. 3i and **Extended data Fig. 8b**). Notably, previous studies demonstrated eIF6's interaction with CD104 in a yeast two-hybrid assay[45], with its ability to localize to intermediate filaments and nuclear matrix[49]. However, this unconventional role of eIF6 in cancer persistence to therapy has not been studied so far. CD104 expression was indeed upregulated in non-NE cell state compared to NE cell state (**Extended data Fig. 8c**). Intriguingly, we also observed increased focal adehesion kinase (FAK) phosphorylation upon chemotherapy treatment (**Extended data Fig. 8d**), as well as in non-NE cell state compared to NE cell state (**Extended data Fig. 8e**), indicative of a potential regulatory role of eIF6 in CD104/FAK signalling axis. We thus utilized proximity ligation assay (PLA) to detect the interaction between eIF6 and CD104/FAK *in situ* followed by our *in-house* PLA analysis pipeline[50] (**Extended data Fig. 8f**). We consistently detected eIF6 protein proximity with FAK (Fig. 3j) or CD104 (**Extended data Fig. 8g**), and the abundance of FAK-eIF6 PLA complexes was significantly increased in H69M cells compared to H69 cells (Fig. 3j). Moreover, eIF6 knockdown substantially reduced the number of FAK-eIF6 PLA complexes, similarly observed in CD104-eIF6 PLA complexes (**Extended data Fig. 8g**). This suggests that chemotherapy-induced eIF6 is in close proximity to integrin-FAK complexes, potentially influencing integrin-mediated downstream signalling in non-NE cell state.

Further transcriptomic analysis revealed a significant downregulation of MAPK pathway gene signature upon eIF6 knockdown (Fig. 3k, left), including MAPK pathway target genes like *DUSP3, DUSP5, DUSP6* and *MAP2K1* etc (Fig. 3k, right). In line with this, eIF6 knockdown prevented the increased phosphorylation of ERK1/2 in non-NE cell state, with a mild effect on the autophosphorylation of FAK (Fig. 3l **and Extended data Fig. 8e**). This further indicates that eIF6 may function as a protein promoting signalling transduction in the CD104/FAK-ERK1/2 axis. Interestingly, a recent work also demonstrated eIF6's interaction with FAK for the local activation of ERK1/2 at focal adhesions in endothelial cells responding to mechanical forces[51]. Finally, carboplatin/etoposide treatment induced ERK1/2 phosphorylation was partially inhibited by eIF6 knockdown in RPM-derived mouse cell lines (**Extended data Fig. 8h**). In accordance, eIF6 knockdown partially decreased ERK1/2 phosphorylation induced by HGF treatment, known to promote a non-NE transdifferentiation in SCLC (**Extended data Fig. 8i**). Additionally, MEK inhibitor cobimetinib partially inhibited the increased phosphorylation of ERK1/2 in H69M cells (**Extended data Fig. 8j**). Overall, chemothereapy-induced eIF6 functions in a non-classical manner by dissociating from the ribosome pool and interacting with integrin/FAK complexes to activate downstream MAPK pathway in non-NE cell state of SCLC. However, the partial effect on ERK1/2

phosphorylation upon eIF6 knockdown or MEK inhibition suggests the involvement of other potential regulatory mechanisms in MAPK pathway activation.

Clinical relevance of eIF6 moonlight function in therapeutic response

To evaluate the translational potential of this new found insight for the clinical prognostication of SCLC treatment, we procured formalin-fixed, paraffin-embedded (FFPE) tumour samples from a cohort of patients (n = 38) with limited-stage SCLC prior to adjuvant therapies. Utilizing the proximity ligation assay, we aimed to detect the *in situ* interaction of CD104-eIF6 or FAK-eIF6 complexes in patient samples (Fig. 4a). Concurrently, we performed mIF staining of eIF6, ASCL1 and NEUROD1 on consecutive FFPE slides, revealing a heterogeneity of CD104-eIF6 or FAK-eIF6 localization dependent on the expression patterns of eIF6 and ASCL1 within the same patient tumour (Fig. 4b and **Extended data Fig. 9a**). Notably, CD104-eIF6 spots were scarcely detected in ASCL1-high regions (Fig. 4b, 1), whereas an increased abundance of CD104-eIF6 spots was observed in eIF6-high/ASCL1-low regions (Fig. 4b, 2–3). Despite a mild correlation between eIF6 expression and NEUROD1 expression, and an inverse correlation with ASCL1 expression within the sample patient samples, no associations were identified between eIF6 expression and tumour stages or metastatic features in this cohort (Fig. 4c). In contrast, the percentage of CD104-eIF6 PLA-positive cells displayed a negative correlation with the percentage of ASCL1-positive cells and a positive correlation with the percentage of eIF6-positive cells (Fig. 4d). These clinical findings substantiate and extend our observations from *in vitro* experiments and mouse models.

To quantitatively assess eIF6 PLA spots in patient samples, we devised an image-based analysis pipeline (**Extended data Fig. 9b**). Initially, we estimated the Hematoxylin-DAB (H-DAB) staining vector by using QuPath (**Extended data Fig. 9b**) and subsequently implemented a script-based cell and spot segmentation approach. This methodology facilitated the identification of PLA spots at single-cell level (Fig. 4e and **Extended data Fig. 9c**). The utilization of such a digital image analysis aimed to mitigate the subjective limitations inherent in visual semi-quantitative scoring methods, providing an adequate dynamic range to represent biomarker expression in our analysis. In this context, we developed an H-score^{PLA} algorithm wherein individual cells and their sub-cellular CD104-eIF6 or FAK-eIF6 spots were detected. PLA-positive cells were then classified into high (3+), medium (2+) or low (1+) based on our pipeline (Fig. 4f and **Extended data Fig. 9c**). To comprehensively account for the heterogeneity within an SCLC sample, we randomly quantified at least six different regions on the FFPE slide, and each sample's H-score^{PLA} was calculated (Fig. 4f).

Globally, the percentage of eIF6-positive cells exhibited a mild anti-correlation with event-free survival (EFS), while the opposite trend was observed for the percentage of ASCL1-positive cells (**Extended data Fig. 9d**). The H-score^{PLA} of both CD104-eIF6 and FAK-eIF6 strongly anti-correlated with EFS, indicating poorer clinical outcomes when eIF6 functions in a non-classical manner in SCLC (**Extended data Fig. 9d**). A multivariate linear regression was conducted to evaluate the relationship between EFS and the explanatory variables, including age, the percentage of ASCL1-positive cells (ASCL1%), the percentage of

eIF6-positive cells (eIF6%), and H-score^{PLA} of CD104-eIF6 or FAK-eIF6. In multivariate COX analysis, the higher H-score^{PLA} of CD104-eIF6 and FAK-eIF6 was associated with a lower value of EFS, with an odds ratio of -1.59 (95% CI, -1.895, -1.298) for CD104-eIF6 identified as the most significant biomarker in this cohort (**Extended data Fig. 9e**). No significant prognostic value was found for variables such as age, ASCL1% and eIF6%. Furthermore, we did not observe tumour stage dependency of H-score^{PLA} (Fig. 4g). Notably, H-score^{PLA} of CD104-eIF6 exhibited markedly distinct outcomes at a cut-off value of 15 (Fig. 4h-i). Patients with H-score^{PLA} of CD104-eIF6 over 15 demonstrated nearly triple the median EFS compared to those below this threshold (13 months vs. 5.5 months, $p < 0.0001$) (Fig. 4h). Similarly, patients showed a doubling of median overall survival (OS) when their H-score^{PLA} of CD104-eIF6 surpassed 15 (31.93 months vs 15.4 months, $p = 0.0007$) (Fig. 4i). In total, leveraging our H-score^{PLA} algorithm based on the *in situ* detection of eIF6's non-classical function, we identified distinct SCLC patient subgroups with significant clinical outcomes.

Discussion

We reveal a pivotal role for the translation initiation factor eIF6 in the context of SCLC response to first-line chemotherapy. We demonstrate that the clinical administration of SCLC first-line chemotherapy induces the expression of eIF6, contributing significantly to the transdifferentiation of residual persistent cells. This phenomenon is validated in both a genetically engineered mouse SCLC model and limited-stage patient samples, where a noteworthy anti-correlation is observed between eIF6 expression and classical neuroendocrine markers. Interestingly, the upregulated expression of eIF6 is marked by its dissociation from the 60S ribosomal subunit. In turn, eIF6 interacts with the integrin family protein CD104, initiating a CD104/FAK-MAPK signalling axis specifically in non-neuroendocrine SCLC cells. This non-canonical role of eIF6 suggests an intricate regulatory mechanism within the signalling pathways governing cellular fate. The dissociation of eIF6 from ribosomes contributes to the mitigation of active translating 80S ribosome assembly in non-neuroendocrine SCLC cells, resulting in a coordinated downregulation of global translation activity in the transdifferentiated SCLC cells. In the context of clinical outcomes, the correlation between eIF6 expression alone and poorer clinical outcomes is found to be only mild. However, our innovative approach involves *in situ* quantification of eIF6 interaction with CD104, utilizing a PLA-based scoring method. This method demonstrates a robust correlation with clinical outcomes, providing a more nuanced understanding of the functional implications of eIF6 in SCLC. Moreover, genetic knockdown of eIF6 proves effective in preventing the persister-like transdifferentiation of SCLC cells, particularly in response to chemotherapy or factors associated with EMT. This intervention not only impedes the transdifferentiation process but also enhances the sensitivity of SCLC cells to first-line chemotherapy.

The concept of drug-tolerant persister cells, originally identified as a subpopulation exhibiting slow or non-cycling states under chemotherapeutic pressure[1], aligns with our findings. Previous research underscored the intricate relationship between ribosome-mediated translation and cell proliferation in melanoma drug-tolerant persister cells[15]. However, the regulatory role of translation in persister-like

lineage conversion remained unexplored until our study. In the SCLC context, where treatment failure is often linked to the emergence of a refractory variant with non-neuroendocrine characteristics[8,35,39], we identify a global translation remodelling during the continuum of SCLC tolerant transdifferentiation. Notably, eIF6 emerges as a key regulator in this process by promoting the MAPK signalling pathway. Nevertheless, we acknowledge that eIF6 may not be the sole factor influencing phosphor-ERK signalling in non-NE SCLC. The compelled overexpression of KRasV12 induces the de-differentiation of NE cells towards a more non-NE cell state, as demonstrated by previous research[52]. Recent studies have indicated that the heightened activation of RAS, MEK, or ERK may potentially impede neuroendocrine differentiation in small-cell lung carcinoma (SCLC) and hinder the growth of SCLC NE cells[53]. Considering that RAS exhibits context-dependent capabilities of either suppressing or activating integrin signalling[54], contingent upon the cellular context and the specific integrins involved, it becomes intriguing to further investigate the interplay between eIF6 and this small GTPase.

The molecular stratifications of SCLC, focusing on lineage-defining transcription factors such as ASCL1, NEUROD1, and POU2F3, have been extensively studied for their correlation with therapeutic responsiveness[44,55]. Our study introduces an additional layer of stratification, emphasizing the prognostic value of eIF6 moonlight function. However, we acknowledge the preliminary nature of our findings, as we only tested the prognostic value in limited-stage patient samples. Prospective clinical studies in extensive-stage SCLC are warranted to validate and extend the clinical applicability of our findings. In summary, our study unravels a novel mechanism shaping SCLC subtype plasticity in response to chemotherapeutic treatment, providing a rationale for therapeutic strategies targeting eIF6. The intricate interplay between eIF6, translational regulation, and signalling pathways opens avenues for therapeutic innovation in the treatment of SCLC, offering potential benefits for patient outcomes.

Methods

Ethic statements

All experiment in this study complies with ethical regulations. Animal experiments were performed following the protocol approved by the Animal Ethics Committee of West China hospital, Sichuan University. The use of clinical specimens and data in this study were approved by West China Hospital Sichuan University Biomedical Research Ethics Committee (#2022-36) and written informed contents of all patients were obtained.

Reagents and antibodies

The following chemicals (stored at -20°C or -80°C) were used for experiments where indicated: Carboplatin (Selleckchem #S1215, stock 10mM), Etoposide (Selleckchem #S1225, Stock 50 mM in DMSO), Harringtonine (Abcam #ab141941, stock 100 μg ml^{-1} in DMSO), Cycloheximide (MCE, China, #HY12320, stock 100 mg ml^{-1} in DMSO), GSK-126 (MCE, #HY13470, stock 10 mM in DMSO). The following primary antibodies were used: rabbit anti-RPL7 (Proteintech #14583-1-AP, 1:1,000), rabbit anti-

RPS15 (Proteintech #14957-1-AP, 1:1,000), rabbit anti-phospho-RPS6 (Ser235/236) (CST #2211S, 1:1,000), rabbit anti-phospho-RPS6 (Ser244/247) (Invitrogen #44-923G, 1:1,000), rabbit anti-RPS6 (CST #2217, 1:1,000), rabbit anti-eIF6 (CST #3263, 1:1,000), rabbit anti-phospho-FAK (Tyr397) (CST #8556T, 1:1000), mouse anti-FAK (Santa Cruz, #sc-1688, 1:200), rabbit anti-phospho-Akt (Ser473) (CST #4060, 1:1,000), rabbit anti-Akt (CST #9272, 1:1,000), rabbit anti-phospho-Erk1/2 (CST #4376S, 1:1,000), rabbit anti-Erk1/2 (CST #9102S, 1:1,000), rabbit anti-c-Myc (CST #18583, 1:1,000), rabbit anti-N-Myc (D4B2Y) (CST #51705, 1:1,000), rabbit anti-ASCL1 (E6Y1B) (CST #55467, 1:1,000), rabbit anti-NEUROD1 (D90G12) (CST #7019, 1:1,000), rabbit anti-YAP (CST #14074S, 1:1,000), rabbit anti-Vimentin (CST #5741, 1:1,000), rabbit anti-p70 S6 Kinase (CST, #9202, USA, 1:1000), rabbit anti-phospho-p70 S6 Kinase (Thr389) (108D2) (CST, #9234, USA, 1:1000), rabbit anti-4E-BP1 (53H11) (CST, #9644, USA, 1:1000), rabbit anti-phospho-4E-BP1 (Ser65) (CST, #9451, USA, 1:1000), rabbit anti-eIF6 (Proteintech #10291-1-AP, China, 1:100), mouse anti-CD104 (R&D systems, #MAB4060, USA, 1:100 from 500 μg ml^{-1} stock), rabbit anti-NeuroD1 (Abcam #205300, UK, 1:50), Rabbit anti-ASCL1 (BD #556604, USA, 1:100), rabbit anti-β-tubulin (ZSGB-BIO #TA-10, 1:3,000).

SCLC genetic engineered mouse model and adenovirus infection

RPM mice bearing deletions of *TP53*, *Rb1*, and amplification of Myc^{T58A} were purchased from The Jackson Laboratory, stock no. 029971. The induction of SCLC tumours in RPM GEMM has been described previously[35]. Briefly, SCLC tumours were induced in RPM mice at 5–7 weeks of age by intranasal instillation with 1×10^8 plaque-forming units of Ad5-CGRP-Cre (University of Iowa). In situ lung tumour tissue were harvested at 6–8 weeks post-adenovirus infection.

Micro computed tomography Imaging

RPM mice were imaged to monitor tumour development from four weeks after adenovirus induction. Mice were anesthetized with isoflurane and imaged by small animal micro computed tomography (microCT) (PINGSENG Healthcare (KunShan) Inc, China, #NMC-100). Cruiser (version 1.6.9.3) software was used for image collection. Mice were scanned using “mouse visceral scanning” protocol with a tube voltage of 60 KV, a tube current of 0.13 mA, and a transverse FOV of 100 mm. Primary images were processed by Iteration reconstruction algorithm for three-dimensional reconstruction in software Recon (1.6.9.3). The output images with axial, coronal and sagittal planes were visualized and analysed in Avatar (1.6.9.3). When signs of airway thickening or tumour development shown on microCT images, the RPM mice were sacrificed for further analysis.

Generation of mouse SCLC cell line from RPM GEMM and in vitro cell culture

Once tumour developed and detected by microCT, RPM mice were sacrificed and the whole lungs were quickly extracted. After washed in ice-cold PBS, central portion of mouse lung including most of tumour tissue were cut from lungs and minced several times into small pieces in enzymatic digestion media

with sterile scissor. The digestion cocktail consists of 0.33 U/ml collagenase P (Sigma-Aldrich #11213857001), 0.85 U ml^{-1} Dispase (Sigma-Aldrich #D4693), 144 U ml^{-1} DNase I(Sigma-Aldrich #DN25), 100 U ml^{-1} penicillin and 100 μg ml^{-1} streptomycin in 5 ml Roswell Park Memorial Institute (RPMI) medium without serum. Tissue pieces were then incubated in 2.5 ml digestion media at 37°C, 5% CO_2 for 1.5-2 hours with periodic pipetting every 30 minutes until well digested. Digestion was stopped by adding the same volume complete RPMI medium with 10% FBS. The tissue suspension was then filtered through a 70 μm cell strainer (BIOFIL, #CSS013070) and centrifuged for 5 minutes at 2,000 rpm. Cell pellets were re-suspended in 3 ml RBC lysis buffer (Thermo Fisher Scientific, #00-4333-57), incubated at room temperature (RT) for 3 minutes, centrifuged at 1,000 rpm for 3 minutes, re-suspended in complete RPMI culture medium and seeded in T25 cell culture flask (Thermo Fisher Scientific, #156367). After 2-day culture at 37°C, 5% CO_2, SCLC tumour cells in suspension were isolated from adherent stromal cells and reseeded in T25 or T75 culture flask (Thermo Fisher Scientific, #156499) with fresh medium. Following 2-week culture in vitro, these tumour cells transformed from spherical suspension growth to adherence growth. Early-passage cell lines were cultured for less than 3 weeks, and late-passage cell lines were cultured for more than a month. All RPM GEMM derived cell lines were validated by immunoblotting for ASCL1 and MYC.

Xenograft mouse model

For subcutaneous tumour growth of H69, H69 sh_NTC, or H69 sh_eIF6 cells, 1×10^7 cells were implanted subcutaneously on the right lower quadrant of 6- to 8-week-old female immunocompromised *BALB/cNj-Foxn1^{nu}/Gpt* mice from GemPharmatech (Strain No. D000521). Tumour volume was measured with a calliper three times a week and the volume was calculated as follows: V = (length × $width^2$) /2. Based on our animal protocol, the tumours did not exceed 1,500 mm^3 in volume.

Chemotherapy treatment in vivo

Mice bearing H69 cells were randomized and started on the combination chemotherapy when tumour reaching to 400- to 500- mm^3. Mice were treated weekly with carboplatin (60 mg/kg, Selleckchem) in PBS on day1, etoposide (12 mg/kg, Selleckchem) in 70% PEG (MCE, HY-Y0873, USA) in water on day 2, or PBS by intraperitoneal injection (i.p.). Residual tumours were collected 3 weeks after treatment, while regrowth tumours were harvested after tumour relapsed and reached 1,000 mm^3 post 6-weeks-long treatment. For drug response test on H69 sh_NTC and H69 sh_eIF6 cell line-based xenograft, mice with tumour reaching 100–200 mm^3 were started on 3 weeks combination chemotherapy as described above.

Preparation of mouse subcutaneous tumour for analysis

Mice were sacrificed and tumours were dissociated mechanically with sterile scissors, washed in PBS, and minced into small pieces. For protein extraction, tumour pieces were placed into a 2 ml homogenizing CK14 centrifuge tubes (Precellys, France, #P000912-LYSK0) with grinding beads and 300 μl ice-cold RIPA lysis buffer (CST #9806) supplemented with protease inhibitor cocktail (Solarbio, China

#P6730) and phosphatase inhibitors (Solarbio, China #P1260). The tissue was then grinded by homogenizer Bioprep-24R (Allsheng, China) for 5 cycles with 30 seconds on and 30 seconds off for each cycle at 4°C, 4,260 rpm. Following grinding, tumours were placed on ice for at least 30 minutes for further lysis and then centrifuged for 10 minutes at 4°C, 17,000 g to dissociate the clear supernatant containing protein.

Human cell lines and cell culture

Human SCLC cell lines NCI-H69, NCI-H82, NCI-H196, NCI-H146, and DMS114 were purchased from the American Type Culture Collection (ATCC) and authenticated by STR. H69M cell lines were generated in the laboratory from H69 cells and have been described previously[25]. 1×10^6 H69 cells were seeded in 60 mm dishes (NEST, China, #705001) with complete 1640 culture medium containing 40 ng ml^{-1} human recombinant HGF (Peprotech, #100-39H). Fresh medium with HGF was changed every 2 days for 14 days and the adherent cells were isolated and maintained in culture for 1 month. The generated H69M cell line was confirmed by the morphologic changes under light microscopy and immunoblot analysis. All cell lines were incubated at 37°C with 5% CO2 in a humidified environment and cultured in RPMI-1640 medium (Gibco #C11875500CP) supplemented with 10% fetal bovine serum (FBS, Lonsera #S711-001S), except for 293T cells which were cultured in complete DMEM (Gibco #C11995500CP). All cell lines were subjected to periodic PCR-based testing (SoutherBiotech #13100-01) to confirm their mycoplasma-free status.

SCLC cell transdifferentiation assay

For Fig. 3e, early-passage mouse SCLC cells were infected with lentivirus containing eIF6 shRNA (sh_eIF6) or non-targeting control (sh_NTC). 72 hours after infection, mouse SCLC cells of each group were then plated at 1×10^5 per well in six-well plates. Seven days later, cells were stained with crystal violet for visualization. Bright-field images were captured by using Nikon Eclipse 80i microscope (Nikon, Japan). For extended data Fig. 7c-d, 1×10^5 H69_shNTC or H69_sh_eIF6 cells were seeded per well of six-well plate in 2.5 ml complete medium containing 40 ng ml^{-1} HGF or 5 μM EZH2 inhibitor (GSK126) on day 1. Culture medium with 40 ng ml^{-1} HGF or 5 μM EZH2 inhibitor was changed every 48 hours. On day 14, representative bright-field images were captured by microscopy. Following twice washes to remove non-adherent cells, the adherent cells were then stained with crystal violet for quantification of adherent colony numbers.

Clonal formation assay

RPM GEMM derived SCLC cells were seeded at 1×10^5 cells/well in six-well plates for 24 hours, followed by carboplatin and etoposide or vehicle treatment for 72 hours. Cells were maintained in culture without drugs for another 10 days and then stained with crystal violet for visualizing the entire well and calculating the proportion of colony area in each well.

Drug response test

H69 cells, H69M cells, and H196 cells were seeded in 96 well plates at 3×10^4, 5×10^3, and 2×10^3 per well respectively, followed by different concentrations of CE combined chemotherapy for 72 hours. Cell viability was determined by CCK8 assay (MCE #HY-K0301). CCK8 was added to the wells at a final concentration of 10%, and absorbance at 450 nm was measured two hours after incubation.

Flow cytometry

H69 and H69M cells were collected, washed twice in PBS, fixed in 4% PFA for 10 minutes at RT, washed in PBS, permeabilized in 0.5% Triton X-100 for 10 minutes at RT, washed in PBS and incubated with rabbit anti-eIF6 antibody (CST #3263, 1:100) in the dark for 15 minutes at RT. Samples were then washed with PBS and incubated with goat anti-rabbit secondary Antibody (Alexa Fluor 488) (Invitrogen #A-11034) for 30 minutes at RT. After washing, cells were transferred to flow cytometry tubes and analyzed on a Fortessa Flow Cytometer (BD). Data analysis was performed with FlowJo (10.8.1) software. For human SCLC cell flow cytometry analysis, cells were plated at 1×10^6 cells per well in six-well plates and then treated with CE combined chemotherapy for 72 hours. All cells in each well were collected, washed twice in PBS, and incubated with dead cell stain kit (Invitrogen #L34966) at 1:500 in the dark for 30 minutes at room temperature. After washing, cells were fixed with 4% PFA for 15 minutes at RT, washed with PBS and transferred to flow cytometry tubes for analysis as described above.

shRNA plasmid

shRNA in the pLKO.1 lentivirus vector targeting specific genes were purchased from Horizon TRC library. The following shRNA target sequence were used for knockdown experiment: mouse Eif6 (1:TGTCACCACCTGCAATGACTA; 2:GAGAGCGTCTTCAAGCTGAAT), human eIF6 (1: AGAGAACTTCTACAGTGTGTT; 2: ACAGAAGAAATTCTGGCAGAT), non-targeting shRNA (sh_NTC, CAACAAGATGAAGAGCACCAA).

Lentivirus production and virus infection

Lentivirus were made by co-transfection of shRNA lentivirus vector and the packaging plasmid psPAX2 (addgene#12260) and pMD2.G (addgene#12259) through calcium phosphate co-precipitation into 293T cells. Virus-containing supernatants were collected at 48 and 72 hours after transfection, filtered through a 0.45 m filter and aliquoted, then frozen at -80°C. 1×10^6 cells were suspended in 1ml lentivirus with 8 μg ml^{-1} polybrene in each well of six well plates. Virus containing medium was replaced by fresh complete medium 6 hours later. Following 72 hours growth, infected mouse and human SCLC cells were selected in puromycin at 3 μg.ml^{-1} and 1 μg ml^{-1} respectively. The knockdown efficiency was validated by immunoblot after 9–14 days selection. For transdifferentiation blocking test, early-passage RPM derived cells were seeded at 1×10^5 cells per well in six well plates 3 days after sh_NTC or sh_eIF6 lentivirus infection. Following 7 days culture, cells were stained with crystal blue for visualizing with bright field microscopy.

Polysome profiling

Cells were incubated with 100 μg ml^{-1} cycloheximide for 5 min at 37°C, washed twice with ice-cold PBS containing 100 μg ml^{-1} cycloheximide, scraped into centrifuge tubes with 5 ml PBS and centrifugated at 37°C 300 g for 5 minutes. Cell pellets were then lysed in 500 μl hypotonic buffer (5 mM Tris-HCl pH 7.5, 2.5 mM $MgCl_2$, 1.5 mM KCl, 100 μg ml^{-1} cycloheximide, 2 mM DTT, 100 U/ml RNase inhibitor (Promega), 0.5% sodium deoxycholate, 0.5% Triton X-100). The samples were kept on ice for 30 minutes and then centrifuged at 4°C 17,000 g for 10 minutes to remove cell debris. An equivalent amount of ribosomes from each extract were resolved on 5–60% linear sucrose gradient containing 20 mM HEPES (pH 7.6), 5 mM $MgCl_2$, 100 mM KCl, 100 mg/ml cycloheximide, 100 U/ml RNase inhibitor and centrifuged at 36,000 rpm for 2 hours at 4°C in a SW40 rotor in an Optima XPN-100 ultracentrifuge (Beckman Coulter). Gradients were fractionated by a Biocomp Gradient Station fractionator with continuous monitoring of the absorbance at 254 nm. All the polysome plots were proceeded in MATLAB (Mathworks, USA).

Harringtonine run-off assay

Harringtonine run-off assay had been described[30]. Ribosomes run off the mRNA and the rate of polysome loss is measured using sucrose density gradient centrifugation. H69, H69M and H196 cells were treated with 2 μg ml^{-1} harringtonine at 37°C for 3 minutes, followed by incubation with 100 μg ml^{-1} cycloheximide for 5 min at 37°C. Lysates were prepared by scraping the cells into 5 mM Tris-HCl pH 7.5, 2.5 mM $MgCl_2$, 1.5 mM KCl, 100 μg ml^{-1} cycloheximide, 2 mM DTT, 100 U/ml RNase inhibitor (Promega), 0.5% sodium deoxycholate, 0.5% Triton X-100. An equivalent amount of protein from each extract was resolved on 5–50% sucrose gradients.

Ribosome-bound eIF6

H69 and H69M cells were collected and lysed in hypotonic buffer. 800 μl cell lysate of H69 or H69M cells balanced according to total ribosomes were resolved on 1200 μl 30% sucrose cushion containing 20 mM HEPES (pH 7.6), 5 mM $MgCl_2$, 100 mM KCl, 100 mg/ml cycloheximide, 100 U/ml RNase inhibitor and centrifuged at 500,000 g (Beckman Coulter, The Optima MAX XP Ultracentrifuge) for 30 minutes at 4°C in Quick-Seal centrifuge tubes (Beckman Coulter, #344625) in MLA-150 rotor. 1600 μl of supernatant (F1) and 400 μl of remaining (F2) were collected separately for protein extraction using methanol precipitation. Protein extracts of each sample were then re-suspended in the same amount of RIPA (CST) and sample buffer (bio rad), and the same volume of sample F1 and F2 in H69 or H69M cells were used for immunoblotting.

Immunoblotting

Cells were washed twice with ice-cold PBS and lysed in a RIPA lysis buffer (CST #9806S) supplemented with 1 μM DTT, 1 mM PMSF (Solarbio, China #P0100), a protease inhibitor cocktail (Solarbio #P6730) and phosphatase inhibitors (Solarbio, China #P1260). Soluble cell extracts were quantified with Bicinchoninic acid (BCA) assay (Solarbio, China #PC0020) according to manufactories' protocol prior to supplementing with 4X laemmli sample buffer (Bio-Rad) and boiling for 10 minutes at 95°C. An equal amount of protein was resolved by 10% SDS gel electrophoresis with Tris/glycine/SDS running buffer,

transferred onto nitrocellulose membranes using Tris/glycine transfer buffer, blocked with 5% milk for 1 hour and probed with indicated primary antibodies overnight at 4°C. Membrane were washed 3 times in PBST, incubated with gout anti-mouse or anti-rabbit horseradish peroxidase-conjugated (HRP) secondary antibodies (ZSGB-BIO #ZB2301, #ZB2305 respectively) at a 1:5,000 dilution in 5% milk for 1 hour at room temperature, washed with PBST for 3 times, then detected with ultra-sensitive ECL chemiluminescence substrate (4A biotech, #4AW011). Protein was visualized by exposure in a ChemiDoc MP imaging system (Bio-Rad) and quantified with Image Lab (Bio-Rad).

Immunohistochemistry and multiplexed immunofluorescence

The tissue was fixed in 4% paraformaldehyde (PFA, Beyotime Biotechnology) for 6–16 hours at room temperature, washed in PBS, transferred to 75% ethanol, and embedded in paraffin within 1 week after surgical resection. 4 μm Formalin-fixed paraffin embedded (FFPE) sections were dewaxed and rehydrated followed by antigen retrieval with EDTA buffer (pH 9.0, ZSGB-BIO #ZLI9069) at 100°C for 20 minutes. For IHC, slides were quenched with hydrogen peroxide for 10 minutes and blocked with goat serum (ZSGB-BIO #ZLI9056) for 30 minutes at RT. Slides were then incubated with rabbit anti-ASCL1 (E6Y1B) (CST #55467, 1:100) or rabbit anti-eIF6 (CST #3263, 1:100) overnight at 4°C, washed three times, and incubated with gout anti-rabbit (ZSGB-BIO #PV-6000) for 40 minutes at RT. DAB (CST) was used for staining immunocomplex and hematoxylin was used for counterstaining. For multiplexed immunofluorescence (mIF), Opal Polaris 7-Color Automation IHC kit (Akoya) was used according to manufacturer's instructions. The following primary antibodies were used for mIF: rabbit anti-eIF6 (CST #3263, 1:50), NeuroD1 (Abcam #205300, 1:50), ASCL1 (BD #556604, 1:100). Bright filed images of IHC and H&E were captured by VS200 whole slide scanner (Olympus LS). mIF slides were imaged using Vectra Polaris imaging system (Akoya). All analyses were carried out using QuPath (v 0.4.3). Tumour area of each slide was delineated by a trained pathologist in a blinded fashion. The intensity and frequency of positively stained cells within tumours were quantified for calculating the proportion of ASCL1+, NeuroD1+, and eIF6 + cells.

Proximity ligation assay

For immunofluorescence PLA of SCLC cell lines, 1×10^5 H69, H69M_shNTC or H69M_sh700 cells were fixed on cell culture slides with 4% PFA for 10 minutes at RT separately. Cells were then permeabilized in 0.2% PBS-Tween 20 for 10 minutes at RT. Fluorescent PLA on cells was performed using Duolink in situ detection reagent (far red, Sigma-Aldrich, #DUO92008) according to manufacturer's protocol. Briefly, slides were blocked with blocking solution for 30 minutes at RT and incubated with rabbit anti-eIF6 (Proteintech #10291-1-AP, 1:100) and mouse anti-FAK (Santa Cruz #sc1688 1:100) or rabbit anti-eIF6 and mouse anti-CD104 (R&D systems, #MAB4060, 1:100 from 500 μg ml^{-1} stock) at 4°C overnight. Duolink in situ anti-rabbit minus and anti-mouse plus (Sigma-Aldrich, #DUO92008, DUO92001) were used as secondary antibodies. Then, slides were incubated with ligase in ligation buffer and polymerase in

amplification buffer sequentially. Cells were stained with phalloidin (FITC, ABclone #RM02836, 1:1,000 in PBS) for 15 minutes at RT prior to mounting with Duolink mounting medium with DAPI (Sigma-Aldrich, #DUO82040). Immunofluorescence images were taken by Nikon Eclipse 80i upright microscope (Nikon) and analysed using Qupath (v 0.4.3). Positive PLA signal (red points) was identified and quantified in each cell segmented based on DAPI and phalloidin (Fig. 3j). For bright-filed PLA, FFPE slides were made and retrieved with EDTA buffer (pH 9.0) following the same protocol in IHC and multiplex IF. After blocking, primary antibody incubation, PLA probe incubation, ligation, and amplification (procedure similar to immunofluorescence PLA), slides were incubated with HRP labelled probe and substrate solution for staining development, followed by counterstaining with hematoxylin (Sigma-Aldrich, #DUO92012). All slides were then imaged by VS200 whole slide scanner (Olympus LS) and analyzed using QuPath (v 0.4.3). Cells with positive PLA signal (red points) were identified and quantified within tumours for calculating percentage of CD104-eIF6 positive cells (Fig. 4d, e). Cells were then classified into PLA high (3 or more spots within one cell), PLA medium (2 spots within one cell), PLA low (1 spot within one cell) and PLA negative (no spot) cells.

Patient data

Clinical information and tumour samples of SCLC patients were collected from the Department of Thoracic Surgery and Department of Pathology, West China Hospital (WCH). 85 SCLC patients with enough paraffin embedded tumour samples for FFPE slides between 2012 to 2020 were first included. Based on the following inclusion and exclusion criteria, 38 patients were finally enrolled in our retrospective cohort (**Supplementary Table 4**). The inclusion criteria: 1) Single lesion; 2) No prior treatment with radiotherapy or chemotherapy; 3) First time undergoing lung surgery; 4) Postoperative pathological diagnosis of SCLC; 5) Availability of regular postoperative follow-up data. The exclusion criteria: 1) Multiple lesions in the lungs; 2) Incomplete clinical information; 3) Prior treatment with radiotherapy or targeted therapy. Event free survival (EFS) in this study was defined as the length of time that a patient remains free of tumour recurrence, tumour metastasis, or death confirmed by imaging or biopsy findings after surgery. Overall survival (OS) in this study was defined as the length of time from surgery to a patient's death.

Public Datasets and RNA-seq data analyses

Gene expression data of SCLC patients in this study originated from publicly available clinical SCLC datasets: comprehensive SCLC genomic profiling (GSE69091)[21], Chemotherapy-treatment and tumour relapse cohort (dbGAP with accession #PHS001049, https://www.ncbi.nlm.nih.gov/gap/?term = PHS001049)[14], and IMPower133 cohort dataset (EGAD00001006927, https://ega-archive.org/datasets/EGAD00001006927)[23]. RPM and RPR2 mouse transcriptomic datasets were obtained from GSE89660[35]. Numeric expression values of clinical cases and mouse models are normalized and log2 transformed for further analysis. SCLC gene expression data from IMPower 133 trial were clustered into NE and non-NE subgroups through NMF algorithm (NMF R package)[56]. To optimally identify differentially expressed genes, the cluster number was chosen based on Cophenetic

correlation coefficient maximization. Four clusters were eventually selected based on SCLC transcriptomes. ASCL1, NeuroD1, POU2F3, and YAP1 emerged as crucial factors for clustering, and NMF-derived gene signatures are shown in extended data Figs. 1a-b. Upregulated genes in relapsed vs. treatment naive SCLC patients were used to perform GSEA in Fig. 1b through GSEA software version 4.1.0. Ranking algorithm was set as signal2noise. Hallmark and GO. BP (version 202302) were chosen as the gene set database. Differential expression of specific genes across SCLC transcript subtypes was performed on count per million (CPM) with GraphPad Prism 9.5.1 in Fig. 2e and extended data Fig. 5f-i. Comparison of gene expression of c-Myc, eIF6 and ASCL1 between RPM and RPR2 tumour was normalized following the description as shown in the corresponding literature[35]. The gene expression correlation of ASCL1 and eIF6 in IMPower 133 cohort was calculated on transcripts per million (TPM) by Pearson correlation coefficient.

Polysome RNA-seq and cytoplasmic RNA-seq

Polysome-bound RNA was extracted from sucrose-based fractions using TRIzol LS (ThermoFisher) according to manufacturer's protocol and was quantified by Nanodrop microvolume spectrophotometers (ThermoFisher Scientific). Cytoplasmic RNA was extracted from cell lysate in hypotonic buffer using TRIzol LS and was quantified by Nanodrop as well. Polysome-bound RNA and cytoplasmic RNA of each experiment were submitted to Novogene Co., Ltd. Sequencing libraries were generated using NEBNext Ultra RNA Library Prep Kit for Illumina (NEB, USA, Catalog #: E7530L) following manufacturer's recommendations and index codes were added to attribute sequences to each sample. The qualified libraries were pooled and sequenced on Illumina platforms with PE150 strategy in Novogene Bioinformatics Technology Co., Ltd (Beijing, China), according to effective library concentration and data amount required.

Transcriptome and Translatome analysis

Trimmed sequence reads were mapped to GRCh38/hg38 using STAR and count data were generated using HTSeq. Gene set enrichment analysis of cytoplasmic RNA-seq was implemented by using GSEA software version 4.1.0. GSEA was performed using Hallmark EMT, 'Top 100 neuroendocrine genes' (Supplementary Table 3)[43] and KEGG in Fig. 3a,b,k respectively. Differential gene expression between H69M sh_NTC and sh_eIF6 cells in a specific gene set was normalized by z-score and performed in heatmap.

Gene expression count was used for paired analysis of cytoplasmic RNA-seq (transcriptome) and polysome RNA-seq (translatome) with R software, which was reported in previous publications[15]. Genome-wide assessment of differential translations with polysome profiling data was calculated with Xtail package[57]. In brief, Xtail assumes that mRNA abundances in polysome (actively translated mRNA) are not synchronized with mRNA expressions when a gene is subjected to translational dysregulation under certain experimental or physical conditions. Translation efficiency (TE) of each gene can be calculated by comparing difference between the log2FoldChange of polysome mRNA and cytoplasmic

mRNA. Hence, genes whose expression was only regulated at transcription level or only at translation level could be identified.

Tandem mass tag-based Mass Spectrometry

Tandem mass tag (TMT) based Mass spectrometry for comparing groups in different polysome fractions has been described previously[58]. After polysome profiling, sucrose-based fractions of monosome (M), light polysome (LP) and heavy polysome (HP) in H69 and H69M cells were pooled together respectively. Each merged component was mixed with four times volume of methanol, three times volume of ultra-pure water and the same volume of chloroform, followed by centrifuging at 17,000 g for 5 minutes. After separation by centrifugation, the top water layer was removed carefully, and the same volume of methanol was added to the remain. The protein was then precipitated by centrifugation at 17,000 g for 15 minutes. Protein pellets were resuspended in DB dissolution buffer (8 M Urea, 100 mM TEAB, pH 8.5), followed by 5 minutes of ultrasonication on ice. The lysate was added with 1 M DTT to react for 1 h at 56°C, and subsequently alkylated with sufficient iodoacetamide for 1 h at room temperature in the dark followed by ice-bath for 2 minutes. Protein concentration of each sample was quantified by BCA assay according to the instruction of Bradford protein quantity kit (Thermo Fisher Scientific).

The volume of each protein sample was made up to 100 µl with DB dissolution buffer (8 M Urea, 100 mM TEAB, pH 8.5). Samples were mixed and digested with trypsin and 100 mM TEAB buffer at 37°C for 4 h, and then were added with trypsin and $CaCl_2$ for digestion overnight. Digested sample was mixed with formic acid for adjusting pH under 3 and centrifuged at 12,000 g for 5 min at room temperature. The supernatant was slowly loaded to the C18 desalting column, washed with washing buffer (0.1% formic acid, 3% acetonitrile) 3 times, then eluted with elution buffer (0.1% formic acid, 70% acetonitrile). The eluents of each sample were collected and lyophilized.

For TMT labelling, 50 µg of each sample was added with 100 µL of 0.1 M TEAB buffer to reconstitute, followed by adding 41 µl of acetonitrile-dissolved TMT labelling reagent. Sample was mixed thoroughly with shaking for 2 h at room temperature. Then, the reaction was stopped by adding 8% ammonia. All labelling samples were then mixed with equal volume, desalted, and lyophilized. Mobile phase A (2% acetonitrile, adjusted pH to 10.0 using ammonium hydroxide) and B (98% acetonitrile) were used to develop a gradient elution. The lyophilized powder was dissolved in solution A and centrifuged at 14,000 g for 20 min at 4°C. The sample was fractionated using a C18 column (Waters BEH C18, 4.6 × 250 mm, 5 µm) on a Rigol L3000 HPLC system, and the column oven was set to 45°C. The elutes were monitored at UV 214 nm, collected for a tube per minute and combined into 10 fractions finally. All fractions were dried under vacuum, and then, reconstituted in 0.1% (v/v) formic acid (FA) in water. UHPLC-MS/MS analyses were performed using an EASY-nLCTM 1200 UHPLC system (Thermo Fisher, Germany) coupled with an Q ExactiveTM HF-X (Thermo Fisher, Germany). The separated peptides were analyzed by Q ExactiveTM HF-X mass spectrometer, with ion source of Nanospray FlexTM (ESI), spray voltage of 2.3 kV

and ion transport capillary temperature of 320°C. Full scan ranges from m/z 350 to 1500 with a resolution of 60000 (at m/z 200), an automatic gain control (AGC) target value was 3×10^6 and a maximum ion injection time was 20 ms. The top 40 precursors of the highest abundant in the full scan were selected and fragmented by higher energy collisional dissociation (HCD) and analyzed in MS/MS, where resolution was 45,000 (at m/z 200) for 10 plex, the automatic gain control (AGC) target value was 5×10^4 the maximum ion injection time was 86 ms, a normalized collision energy was set as 32%, an intensity threshold was 1.2×10^5, and the dynamic exclusion parameter was 20 s.

Analysis of Mass Spectrometry data

The resulting spectra from each run were searched separately against homo_sapiens_uniprot_2022_9_5.fasta.fasta (204961 sequences) database by the search engines: Proteome Discoverer (PD, Thermo, HFX and 480). The searched parameters are set as follows: mass tolerance for precursor ion was 10 ppm and mass tolerance for product ion was 0.02 Da. Carbamidomethyl was specified as fixed modifications, Oxidation of methionine (M) and iTRAQ/TMT plex were specified as dynamic modifications. Acetylation, iTRAQ/TMT plex, Met-loss and Met-loss + Acetyl were specified as N-Terminal modification. A maximum of 2 miscleavage sites were allowed.

In order to improve the quality of analysis results, the software PD further filtered the retrieval results: Peptide Spectrum Matches (PSMs) with a credibility of more than 99% were identified PSMs. The identified protein contains at least 1 unique peptide. The identified PSMs and protein were retained and performed with FDR no more than 1.0%. The protein quantitation results were statistically analysed by T-test. The proteins whose quantitation was significantly different between H69M and H69 groups, ($p < 0.05$ and $|\log_2 FC| > 1$[fold change, FC]), were defined as differentially expressed proteins (DEP). DEPs were used for Volcanic map analysis, cluster heat map analysis and enrichment analysis of GO, IPR and KEGG. Mass spectrometry data from M, LP and HP fractions were grouped together in H69 or H69M cells for principal component analysis (Fig. 1i). All ribosome protein intensity was log2 transformed prior to conducting standard linear regression between H69 and H69M cells in different fractions (M, LP, HP).

Statistics

Statistical analysis was carried out by using GraphPad Prism (v 9.5.1). Data are presented as mean ± SEM or mean ± SD. All pairwise comparisons were assessed by unpaired two-tailed Student's t-test unless otherwise stated. Log-rank test and multivariate linear regression were used for analysing patients' survival data. *P* values < 0.05 were considered significant.

Declarations

Data availability

RNA-seq data that support the findings of this study have been deposited in the Gene Expression Omnibus under accession codes GSE262597. The mass spectrometry proteomics data have been

deposited to the ProteomeXchange Consortium via the iProX partner repository with the dataset identifier PXD051035.

Acknowledgements

S.S. acknowledges grant support from National Natural Science Foundation of China (grant no. 82172794) and from National Clinical Research Center for Geriatrics, West China hospital, Sichuan University (grant no. Y2022JC002). L.L. acknowledges grant support from National Key Research and Development Program of China (grant no. 2022YFC3400405). L.L. acknowledges financial supports, ZYGD18021, ZYJC21002 from 1.3.5 Project for Disciplines of Excellence, West China Hospital, Sichuan University. L.L. acknowledges grant support 2021YFS0024 from the major research project of Sichuan Province, China. M.C. acknowledges grant support from Agence nationale de la recherche of France (grant no. ANR-23-CE14-0023). We thank Li Li, Fei Chen, Chunjuan Bao and Yang Deng from Institute of Clinical Pathology, West China hospital of Sichuan University for their technical support with histological staining. We thank Prof. Trudy G Oliver (Duke University, USA) for her generous suggestions for the RPM mouse model.

Author contributions

H.P., Z.W. and M.W. are co-first authors, contributed equally. S.S. and H.P. designed the study. S.S., H.P., L.L., Z.W., M.W. and M.C. interpreted the data and wrote the original draft of the manuscript. H.P., Z.W., M.W., Y.W., K.L., performed RNA-seq and polysome profiling. H.P., Z.W., M.W., X.T. and T.L. performed ribosome mass spectrometry. H.P., Z.W. and M.W. performed in vivo experiment. H.P., B.D., Y.W., M.C., D.C. and Y.D. performed bioinformatics analysis. S.S., H.P. and Z.W. performed patient sample multiplex staining and developed image analysis pipeline. S.S., X.Y., L.L. and W.W. performed histopathology analysis. L.X., C.G., Q.P. and L.L. provided administrative support and data resources, collected patient samples. S.S. supervised the overall study, provided strategic oversight and conceived the study.

Competing interests

M.C. is a CSO for BiPer Therapeutics (Strasbourg, France). S.S. reports personal fees from Agence nationale de la recherche (France), Krebsliga Schweiz (Switzerland), KWF Kankerbestrijding (Netherlands) and Shenzhen Medical Academy of Research and Translation (China).

References

1. Shen, S., Vagner, S. & Robert, C. Persistent Cancer Cells: The Deadly Survivors. Cell 183, 860–874, doi:10.1016/j.cell.2020.10.027 (2020).
2. Pu, Y. *et al.* Drug-tolerant persister cells in cancer: the cutting edges and future directions. Nat Rev Clin Oncol 20, 799–813, doi:10.1038/s41571-023-00815-5 (2023).
3. Megyesfalvi, Z. *et al.* Clinical insights into small cell lung cancer: Tumor heterogeneity, diagnosis, therapy, and future directions. CA Cancer J Clin 73, 620–652, doi:10.3322/caac.21785 (2023).

4. Rudin, C. M., Brambilla, E., Faivre-Finn, C. & Sage, J. Small-cell lung cancer. Nat Rev Dis Primers 7, 3, doi:10.1038/s41572-020-00235-0 (2021).
5. Marine, J. C., Dawson, S. J. & Dawson, M. A. Non-genetic mechanisms of therapeutic resistance in cancer. Nat Rev Cancer 20, 743–756, doi:10.1038/s41568-020-00302-4 (2020).
6. Davies, A. H., Beltran, H. & Zoubeidi, A. Cellular plasticity and the neuroendocrine phenotype in prostate cancer. Nat Rev Urol 15, 271–286, doi:10.1038/nrurol.2018.22 (2018).
7. Zou, M. *et al.* Transdifferentiation as a Mechanism of Treatment Resistance in a Mouse Model of Castration-Resistant Prostate Cancer. Cancer Discov 7, 736–749, doi:10.1158/2159-8290.CD-16-1174 (2017).
8. Lim, J. S. *et al.* Intratumoural heterogeneity generated by Notch signalling promotes small-cell lung cancer. Nature 545, 360–364, doi:10.1038/nature22323 (2017).
9. Herzog, B. H., Devarakonda, S. & Govindan, R. Overcoming Chemotherapy Resistance in SCLC. J Thorac Oncol 16, 2002–2015, doi:10.1016/j.jtho.2021.07.018 (2021).
10. Carney, D. N., Mitchell, J. B. & Kinsella, T. J. In vitro radiation and chemotherapy sensitivity of established cell lines of human small cell lung cancer and its large cell morphological variants. Cancer Res 43, 2806–2811 (1983).
11. Wu, Q. *et al.* YAP drives fate conversion and chemoresistance of small cell lung cancer. Sci Adv 7, eabg1850, doi:10.1126/sciadv.abg1850 (2021).
12. Ireland, A. S. *et al.* MYC Drives Temporal Evolution of Small Cell Lung Cancer Subtypes by Reprogramming Neuroendocrine Fate. *Cancer Cell* 38, 60–78 e12, doi:10.1016/j.ccell.2020.05.001 (2020).
13. Duplaquet, L. *et al.* KDM6A epigenetically regulates subtype plasticity in small cell lung cancer. Nat Cell Biol 25, 1346–1358, doi:10.1038/s41556-023-01210-z (2023).
14. Wagner, A. H. *et al.* Recurrent WNT pathway alterations are frequent in relapsed small cell lung cancer. Nat Commun 9, 3787, doi:10.1038/s41467-018-06162-9 (2018).
15. Shen, S. *et al.* An epitranscriptomic mechanism underlies selective mRNA translation remodelling in melanoma persister cells. Nat Commun 10, 5713, doi:10.1038/s41467-019-13360-6 (2019).
16. Boussemart, L. *et al.* eIF4F is a nexus of resistance to anti-BRAF and anti-MEK cancer therapies. Nature 513, 105–109, doi:10.1038/nature13572 (2014).
17. Neal, J. W., Gubens, M. A. & Wakelee, H. A. Current management of small cell lung cancer. Clin Chest Med 32, 853–863, doi:10.1016/j.ccm.2011.07.002 (2011).
18. Gardner, E. E. *et al.* Chemosensitive Relapse in Small Cell Lung Cancer Proceeds through an EZH2-SLFN11 Axis. Cancer Cell 31, 286–299, doi:10.1016/j.ccell.2017.01.006 (2017).
19. Drapkin, B. J. *et al.* Genomic and Functional Fidelity of Small Cell Lung Cancer Patient-Derived Xenografts. Cancer Discov 8, 600–615, doi:10.1158/2159-8290.CD-17-0935 (2018).
20. George, J. *et al.* Evolutionary trajectories of small cell lung cancer under therapy. Nature, doi:10.1038/s41586-024-07177-7 (2024).

21. George, J. *et al.* Comprehensive genomic profiles of small cell lung cancer. Nature 524, 47–53, doi:10.1038/nature14664 (2015).
22. Barbie, D. A. *et al.* Systematic RNA interference reveals that oncogenic KRAS-driven cancers require TBK1. Nature 462, 108–112, doi:10.1038/nature08460 (2009).
23. Gay, C. M. *et al.* Patterns of transcription factor programs and immune pathway activation define four major subtypes of SCLC with distinct therapeutic vulnerabilities. *Cancer Cell* 39, 346–360 e347, doi:10.1016/j.ccell.2020.12.014 (2021).
24. Horn, L. *et al.* First-Line Atezolizumab plus Chemotherapy in Extensive-Stage Small-Cell Lung Cancer. N Engl J Med 379, 2220–2229, doi:10.1056/NEJMoa1809064 (2018).
25. Canadas, I. *et al.* Targeting epithelial-to-mesenchymal transition with Met inhibitors reverts chemoresistance in small cell lung cancer. Clin Cancer Res 20, 938–950, doi:10.1158/1078-0432.CCR-13-1330 (2014).
26. Canadas, I. *et al.* Tumor innate immunity primed by specific interferon-stimulated endogenous retroviruses. Nat Med 24, 1143–1150, doi:10.1038/s41591-018-0116-5 (2018).
27. Bohlen, J., Roiuk, M. & Teleman, A. A. Phosphorylation of ribosomal protein S6 differentially affects mRNA translation based on ORF length. Nucleic Acids Res 49, 13062–13074, doi:10.1093/nar/gkab1157 (2021).
28. Advani, V. M. & Ivanov, P. Translational Control under Stress: Reshaping the Translatome. Bioessays 41, e1900009, doi:10.1002/bies.201900009 (2019).
29. Jobava, R. *et al.* Adaptive translational pausing is a hallmark of the cellular response to severe environmental stress. *Mol Cell* 81, 4191–4208 e4198, doi:10.1016/j.molcel.2021.09.029 (2021).
30. Ingolia, N. T., Lareau, L. F. & Weissman, J. S. Ribosome profiling of mouse embryonic stem cells reveals the complexity and dynamics of mammalian proteomes. Cell 147, 789–802, doi:10.1016/j.cell.2011.10.002 (2011).
31. Genuth, N. R. & Barna, M. The Discovery of Ribosome Heterogeneity and Its Implications for Gene Regulation and Organismal Life. Mol Cell 71, 364–374, doi:10.1016/j.molcel.2018.07.018 (2018).
32. Ceci, M. *et al.* Release of eIF6 (p27BBP) from the 60S subunit allows 80S ribosome assembly. Nature 426, 579–584, doi:10.1038/nature02160 (2003).
33. Jaako, P. *et al.* eIF6 rebinding dynamically couples ribosome maturation and translation. Nat Commun 13, 1562, doi:10.1038/s41467-022-29214-7 (2022).
34. Gandin, V. *et al.* Eukaryotic initiation factor 6 is rate-limiting in translation, growth and transformation. Nature 455, 684–688, doi:10.1038/nature07267 (2008).
35. Mollaoglu, G. *et al.* MYC Drives Progression of Small Cell Lung Cancer to a Variant Neuroendocrine Subtype with Vulnerability to Aurora Kinase Inhibition. Cancer Cell 31, 270–285, doi:10.1016/j.ccell.2016.12.005 (2017).
36. Rudin, C. M. *et al.* Molecular subtypes of small cell lung cancer: a synthesis of human and mouse model data. Nat Rev Cancer 19, 289–297, doi:10.1038/s41568-019-0133-9 (2019).

37. Megyesfalvi, Z. *et al.* Expression patterns and prognostic relevance of subtype-specific transcription factors in surgically resected small-cell lung cancer: an international multicenter study. J Pathol 257, 674–686, doi:10.1002/path.5922 (2022).
38. Schwendenwein, A. *et al.* Molecular profiles of small cell lung cancer subtypes: therapeutic implications. Mol Ther Oncolytics 20, 470–483, doi:10.1016/j.omto.2021.02.004 (2021).
39. Huang, Y. H. *et al.* POU2F3 is a master regulator of a tuft cell-like variant of small cell lung cancer. Genes Dev 32, 915–928, doi:10.1101/gad.314815.118 (2018).
40. Finch, A. J. *et al.* Uncoupling of GTP hydrolysis from eIF6 release on the ribosome causes Shwachman-Diamond syndrome. Genes Dev 25, 917–929, doi:10.1101/gad.623011 (2011).
41. Bankhead, P. *et al.* QuPath: Open source software for digital pathology image analysis. Sci Rep 7, 16878, doi:10.1038/s41598-017-17204-5 (2017).
42. Balanis, N. G. *et al.* Pan-cancer Convergence to a Small-Cell Neuroendocrine Phenotype that Shares Susceptibilities with Hematological Malignancies. *Cancer Cell* 36, 17–34 e17, doi:10.1016/j.ccell.2019.06.005 (2019).
43. Chen, H. Y. *et al.* Regulation of neuroendocrine plasticity by the RNA-binding protein ZFP36L1. Nat Commun 13, 4998, doi:10.1038/s41467-022-31998-7 (2022).
44. Nabet, B. Y. *et al.* Immune heterogeneity in small-cell lung cancer and vulnerability to immune checkpoint blockade. Cancer Cell, doi:10.1016/j.ccell.2024.01.010 (2024).
45. Biffo, S. *et al.* Isolation of a novel beta4 integrin-binding protein (p27(BBP)) highly expressed in epithelial cells. J Biol Chem 272, 30314–30321, doi:10.1074/jbc.272.48.30314 (1997).
46. Valenzuela, D. M., Chaudhuri, A. & Maitra, U. Eukaryotic ribosomal subunit anti-association activity of calf liver is contained in a single polypeptide chain protein of Mr = 25,500 (eukaryotic initiation factor 6). J Biol Chem 257, 7712–7719 (1982).
47. Skabkin, M. A., Skabkina, O. V., Hellen, C. U. & Pestova, T. V. Reinitiation and other unconventional posttermination events during eukaryotic translation. Mol Cell 51, 249–264, doi:10.1016/j.molcel.2013.05.026 (2013).
48. Oughtred, R. *et al.* The BioGRID database: A comprehensive biomedical resource of curated protein, genetic, and chemical interactions. Protein Sci 30, 187–200, doi:10.1002/pro.3978 (2021).
49. Sanvito, F. *et al.* The beta4 integrin interactor p27(BBP/eIF6) is an essential nuclear matrix protein involved in 60S ribosomal subunit assembly. J Cell Biol 144, 823–837, doi:10.1083/jcb.144.5.823 (1999).
50. Shen, S., Girault, I., Malka-Mahieu, H., Robert, C. & Vagner, S. In situ detection of the eIF4F translation initiation complex in mammalian cells and tissues. STAR Protoc 2, 100621, doi:10.1016/j.xpro.2021.100621 (2021).
51. Keen, A. N. *et al.* Eukaryotic initiation factor 6 regulates mechanical responses in endothelial cells. J Cell Biol 221, doi:10.1083/jcb.202005213 (2022).

52. Calbo, J. *et al.* A functional role for tumor cell heterogeneity in a mouse model of small cell lung cancer. Cancer Cell 19, 244–256, doi:10.1016/j.ccr.2010.12.021 (2011).
53. Inoue, Y. *et al.* Extracellular signal-regulated kinase mediates chromatin rewiring and lineage transformation in lung cancer. Elife 10, doi:10.7554/eLife.66524 (2021).
54. Kinbara, K., Goldfinger, L. E., Hansen, M., Chou, F. L. & Ginsberg, M. H. Ras GTPases: integrins' friends or foes? Nat Rev Mol Cell Biol 4, 767–776, doi:10.1038/nrm1229 (2003).
55. Liu, Q. *et al.* Proteogenomic characterization of small cell lung cancer identifies biological insights and subtype-specific therapeutic strategies. *Cell* 187, 184–203 e128, doi:10.1016/j.cell.2023.12.004 (2024).
56. Skoulidis, F. *et al.* Co-occurring genomic alterations define major subsets of KRAS-mutant lung adenocarcinoma with distinct biology, immune profiles, and therapeutic vulnerabilities. Cancer Discov 5, 860–877, doi:10.1158/2159-8290.CD-14-1236 (2015).
57. Xiao, Z., Zou, Q., Liu, Y. & Yang, X. Genome-wide assessment of differential translations with ribosome profiling data. Nat Commun 7, 11194, doi:10.1038/ncomms11194 (2016).
58. Khajuria, R. K. *et al.* Ribosome Levels Selectively Regulate Translation and Lineage Commitment in Human Hematopoiesis. *Cell* 173, 90–103 e119, doi:10.1016/j.cell.2018.02.036 (2018).

Figures

Figure 1.

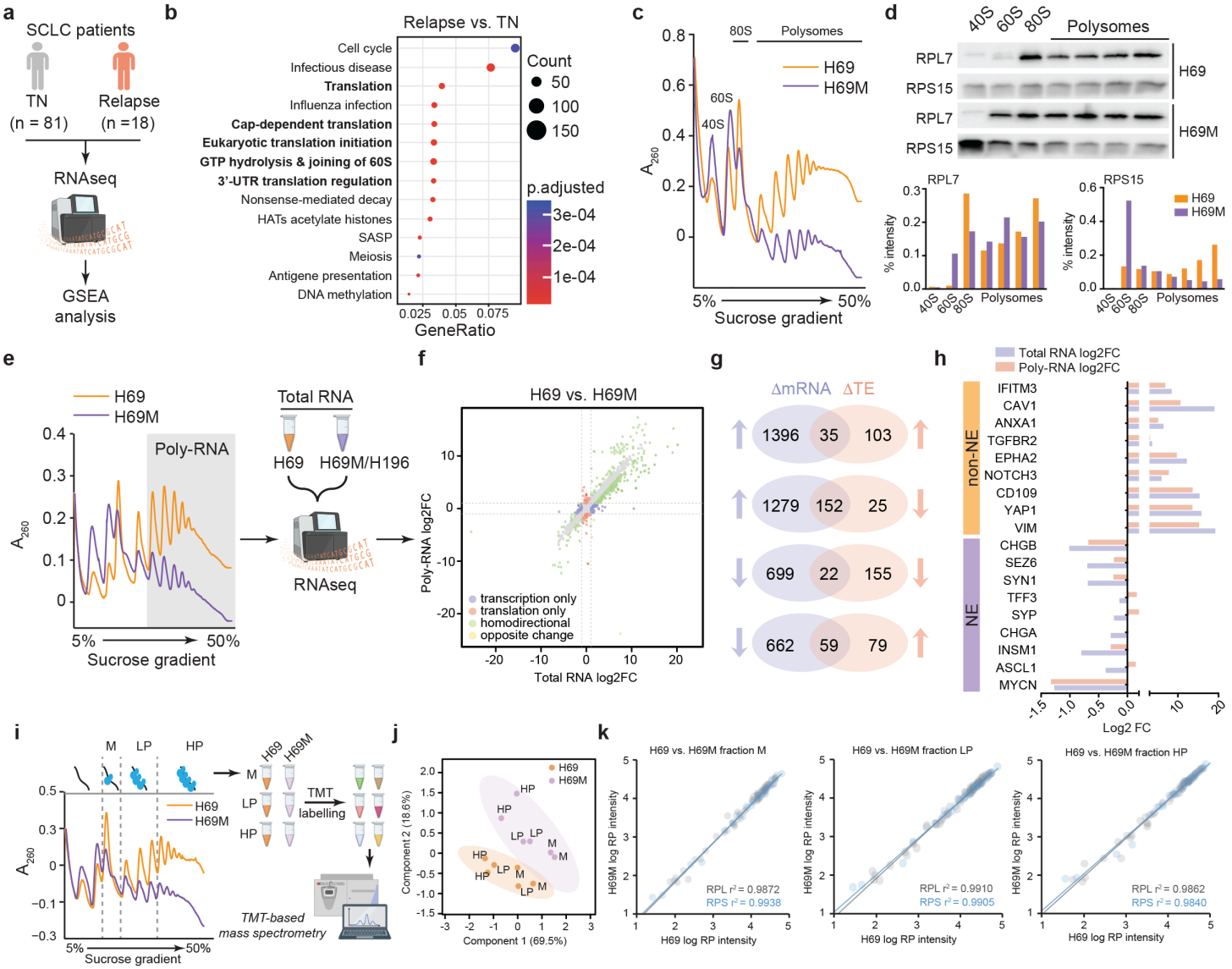

Figure 1

Translational reprogramming upon SCLC transdifferentiation.

a.b, Gene set enrichment analysis (GSEA) of genes upregulated in the relapsed (n=18) versus treatment naive (n=81) tumours from Wagner et al[14]. **c**. Comparison of polysome profiling between H69 and H69M SCLC cells. **d**. Immunoblot and quantification of protein expression of RPL7 and RPS15 in each polysome fraction of H69 and H69M cells. **e.** Combined analysis of poly-RNA sequencing and total RNA sequencing in H69 cells compared with H69M or H196 cells (poly-RNA, Polysome RNA). **f.** Scatterplot depicting gene expression differentiation between H69M and H69 cells on translational and transcriptional level. **g.** Venn diagrams depicting differentially transcribed (DmRNA, log2 fold change >1) or differentially translated (Dtranslation efficiency [DTE]) genes in H69M cells compared with H69 cells. **h**. Expression of non-NE (neuroendocrine) or NE related transcripts from both RNA-seq and polysome RNA-seq data in H69M relative to H69 cells. **i**. Schematic view of TMT-mass spectrometry for polysome profiling. Comparison of protein expression in fraction M, LP and HP between H69 and H69M cells with

TMT-based mass spectrometry (M, monosome; LP, light polysome; HP, heavy polysome). **j**. Principal components analysis of protein in different fraction of H69 and H69M cells. **k**. Scatterplot comparing ribosome protein expression in fraction M, LP, and HP between H69 and H69M cells (Pearson correlation coefficient).

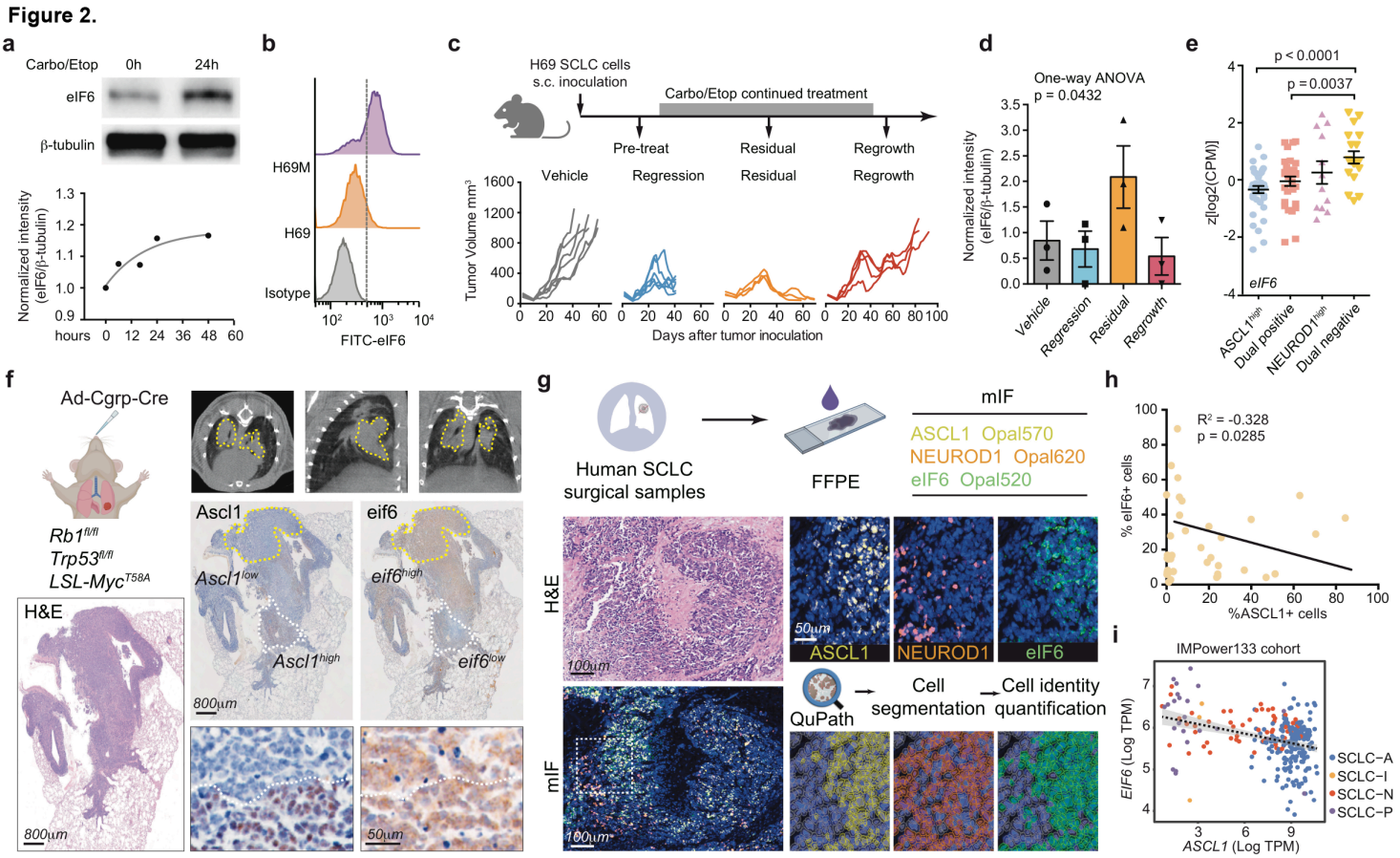

Figure 2

Chemotherapy-induced eIF6 in non-NE cell state of SCLC.

a. Immunoblots of eIF6 and regression curve based on normalized eIF6 intensity showing eIF6 upregulation after chemotherapy for different durations in H69 cells, b-tubulin as loading control (Carbo, carboplatin, 10 mM; Etop, etoposide, 2 mM). **b**. Isotype versus eIF6 expression in H69 and H69M cells with flowcytometry. **c.d**. Quantification of eIF6 protein level with immunoblot in tumours from different groups of H69 cell line xenograft as indicated. **e**. Comparison of eIF6 mRNA expression across ASCL1^{high}, NEUROD1^{high}, dual-positive (ASCL1^{high}NEUROD1^{high}) and dual-negative (ASCL1^{low}NEUROD1^{low}) subtypes from George et al SCLC cohort. **f**. Representative of micro-CT images showing lung tumor formation (in yellow circle) in RPM (*Rb1*$^{-/-}$, *P53*$^{-/-}$, *MYC*^{T58A}) GEMMs infected with Ad-Cgrp-Cre, and representative of H&E and immunohistochemistry (IHC) staining for ASCL1 and eIF6 in lung tumour bed (n=3 mice). **g**. Representative of multiplex IF staining and H&E in the same tumour showing the histopathological distribution of ASCL1, NEUROD1, and eIF6 in human SCLC (n = 38

tumours). **h**. Anti-correlation of proportion of ASCL1+ cells vs. proportion of eIF6+ cells in multiplex IF staining across 38 human SCLC tumours (*p*-value calculated using Spearman's rank correlation coefficient). **i**. Scatterplot depicting negative correlation between eIF6 and ASCL1 on mRNA level with human SCLC RNA-seq data from IMPower133 cohort (n=271). For d, n=3 biological replicates. Data are represented as mean ± SEM. Statistical significance was determined by two tailed unpaired Student's t test. Scale bars, 50 mm.

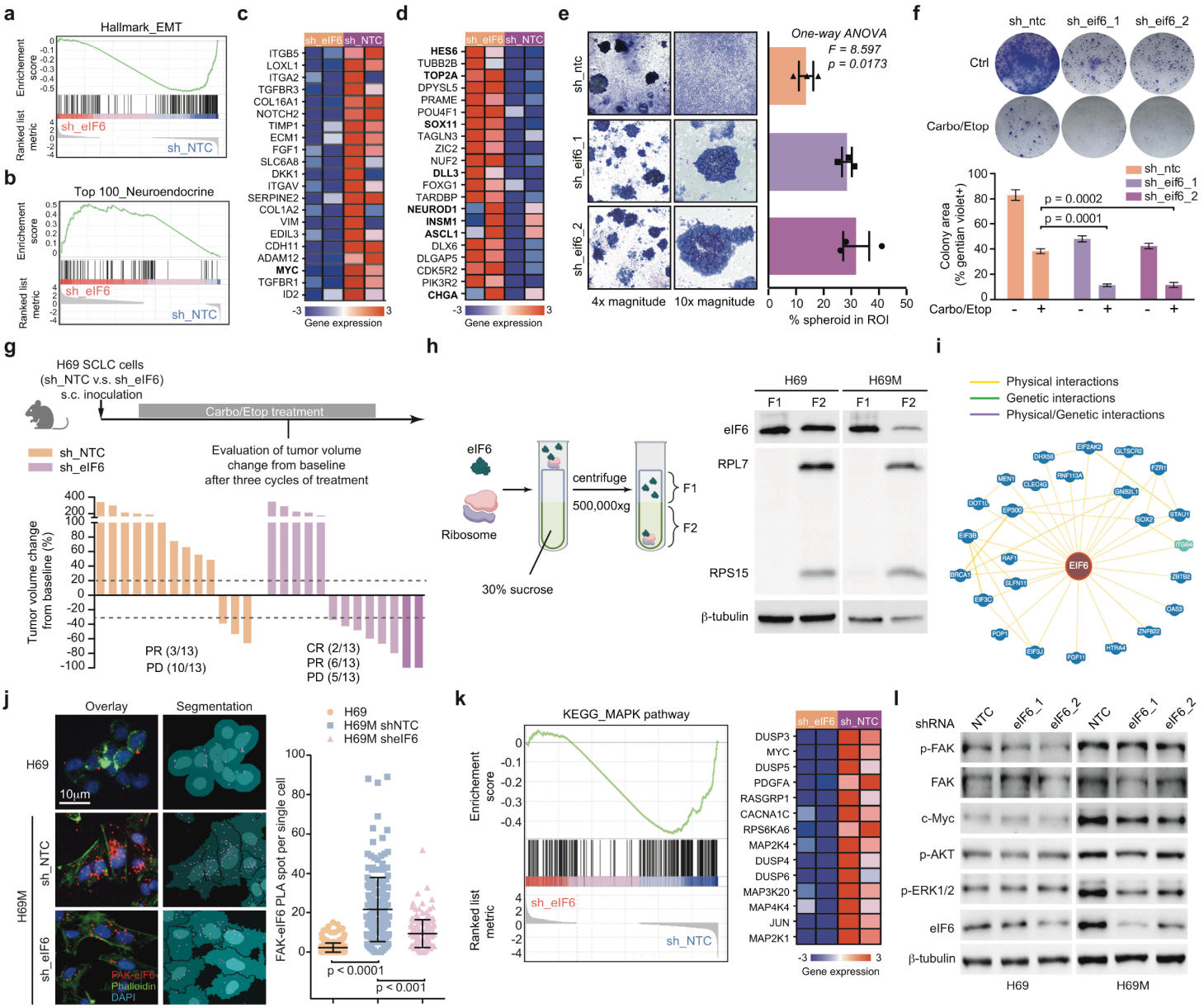

Figure 3

Inhibition of eIF6 mitigates non-NE transdifferentiation and enhances SCLC drug sensitivity

a.b. Gene set enrichment analysis of RNA-seq data for Epithelial-Mesenchymal Transition (EMT) (**a**) and top 100 neuroendocrine genes (**b**) in H69M cells infected with lentivirus containing an eIF6 shRNA

(sh_eIF6) vs. non-targeting control (sh_NTC). **c.d**. Heatmap of RNA-seq data showing enriched (**c**) and deleted (**d**) genes expression in sh_eIF6 H69M cells compared with sh_NTC H69M cells. **e**. Transdifferentiation assay of early-passage mouse SCLC cell lines. Proportion of spheroid-growth clones in each well was calculated and compared across groups using one-way ANOVA. **f**. Representative of crystal violet staining of sh_NTC or sh_eIF6 mouse SCLC cells plated on six-well plates for 10 days after treatment with CE (0.4 mM carboplatin and 0.08 mM etoposide) or vehicle for 72 hours. Colony area was quantified as percentage of gentian violet^{+} area per well. **g**. Tumour volume change from baseline after three cycles of chemotherapy in sh_NTC and sh_eIF6 H69 cell line derived xenografts (n=13 tumours per group). **h**. Schematic view of ribosme-bound eIF6 assay. Cytoplasmic protein was fractioned into free portion (F1) and ribosome binding portion (F2) with sucrose-based ultracentrifugation. Immunoblot showing eIF6 distribution in F1 and F2 of H69 and H69M cells, RPL7, RPS15 and b-tubulin as loading control. **i**. Candidate factors interacting with eIF6 physically or genetically from Biogrid database. **j**. Representative of immunofluorescence images showing interaction of eIF6 and FAK in indicated cells using Proximity ligation assay (PLA) with far red fluorescence. Quantity of eIF6-FAK complex per single cell in H69M shNTC cells vs. H69 or H69M sh_eIF6 cells. **k**. Gene set enrichment analysis and heatmap depicting downregulated genes in MAPK pathway in eIF6 knockdown H69M cells. **l**. Immunoblot indicating the effect of eIF6 knockdown in FAK/ERK singling transduction axis. For e, n=3 biological replicates. For f, n=2 biological independent experiments. Data are represented as mean ± SEM. Statistical significance was determined by two-tailed unpaired Student’s t test unless indicated specifically. Scale bars, 50 mM.

Figure 4.

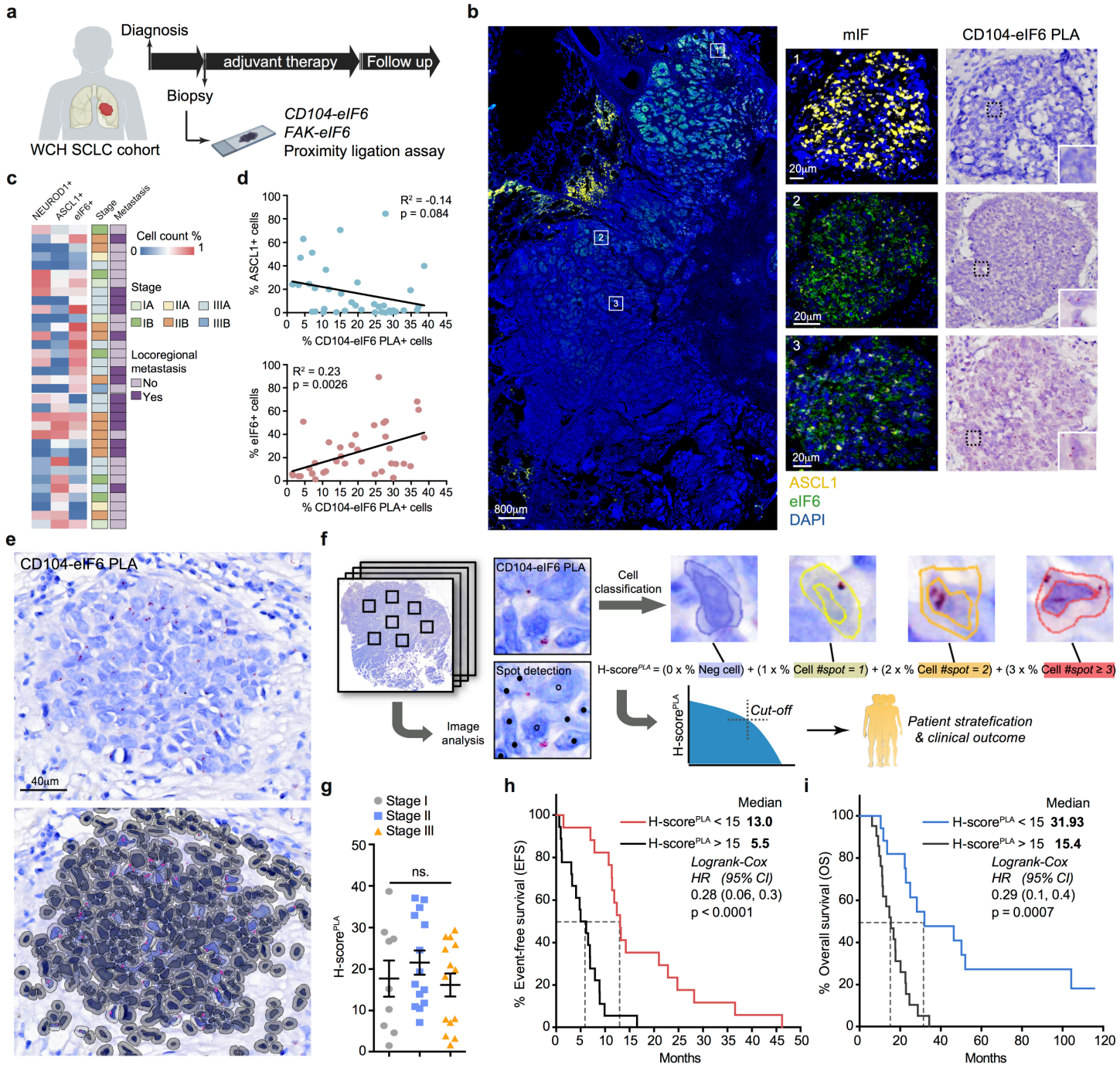

Figure 4

Scoring in situ interaction between eIF6 and CD104/FAK in SCLC clinical samples

a. Schematic view of patient sample collection. Surgical biopsy of 38 limited-stage SCLC patients from West China Hospital was used to detect in situ interaction of eIF6-CD104 or eIF6-FAK with proximity ligation assay. **b**. Representative of multiplex IF staining for eIF6 and ASCL1 and bright field PLA of CD104-eIF6 interaction within the same tumour. **c.** Quantification of eIF6+, ASCL1+, and NEUROD1+ cells

in human SCLC from multiplex IF and their correlation with clinical stages and metastasis status. **d.** Spearmen's rank correlation between proportion of CD104-eIF6 PLA+ cells and proportion of ASCL1+ cells or eIF6+ cells.

e. Representative bright field PLA of CD104-eIF6 (red spot) and segmentation of cells and red spot using Qupath. Scale bars, 40 mM. **f.** Workflow demonstrating PLA image analysis pipeline for patient stratification based on H-score^{PLA}. **g.** Comparison of CD104-eIF6 H-score^{PLA} across different clinical stages. **h-i**. Kaplan-Meier survival curves for (h) event free survival (EFS) and (i) overall survival (OS) based on H-score^{PLA} of CD104-eIF6 (n= in H-score^{PLA} >15 groups and n= in H-score^{PLA} <15 groups). *P* values were calculated from log rank test. For figure g, n=9, 15, 14 patients for stage I, II and III respectively. Data are represented as mean ± SEM. Statistical significance were determined by two-tailed unpaired Student's t test.

Supplementary Files

This is a list of supplementary files associated with this preprint. Click to download.

- eIF6moonlightingdrugV3.0Extdatasupinfo.docx
- supplementaryWBdataresource.pdf